Computation of 3D MHD equilibria with free boundary and diagnostic coil responses for W7-AS

E. Rittger

IPP 2/314

March 1992

MAX-PLANCK-INSTITUT FÜR PLASMAPHYSIK

8046 GARCHING BEI MÜNCHEN

MAX-PLANCK-INSTITUT FÜR PLASMAPHYSIK

GARCHING BEI MÜNCHEN

Computation of 3D MHD equilibria with free boundary and diagnostic coil responses for W7-AS

E. Rittger

IPP 2/314 March 1992

Computation of 3D MHD equilibria with free boundary and diagnostic coil responses for W7-AS

E. Rittger

March 1992

Abstract

The VMEC-DIAGNO code package is tested and used to compute MHD equilibria for W7-AS and the corresponding responses of magnetic field diagnostic coils to the plasma current. It is suggested how to achieve reasonable accuracy and some comparisons with an existing data base are made. A new data base is being established and the possibilities of obtaining relevant plasma parameters by analyzing the diagnostic signals are discussed.

1 Introduction

One way to obtain information on the actual state of the plasma in an experiment is to analyze the response of magnetic field coils to the field generated by the plasma current density. In tokamaks this analysis is fairly simple and routine practice because of their axisymmetry. For stellarators, in contrast, the solution of a 3D ideal MHD equilibrium requires much more computing capacity. Gardner [1] used a steepest descent algorithm which took the VMEC code [2] about 50 hours CRAY–XMP computing time per equilibrium. Since then a preconditioned descent algorithm [2] has been introduced into the VMEC code which reduces the computing time by one to two orders of magnitude. This progress now makes it possible to set up a data bank of W7-AS equilibria and diagnostic coil responses which should help to clarify experimental results. The work on this data bank is now in progress. The testing of the code and some first results are reported in the following.

2 Convergence properties of the code

Before mass production of stellarator equilibria can begin, it must be established with what parameters the code has to be run (and hence what computing capacity it requires) to achieve reasonable accuracy. To introduce these parameters, it should be recalled that VMEC is based on a description of the equilibrium in terms of flux surfaces. The cylindrical coordinates $r(s,u,v)$ and $z(s,u,v)$ which describe these surfaces for N_S values of the normalized flux s from $s = 0$ (axis) to $s = 1$ (boundary) are expanded in sine and cosine series of the poloidal (u) and toroidal (v) coordinates:

$$r(s_j,u,v) = \sum_m \sum_n r_{jmn} \cos(2\pi(mu - nv)),$$

$$z(s_j,u,v) = \sum_m \sum_n z_{jmn} \sin(2\pi(mu - nv)).$$

A similar expansion holds for the magnetic field:

$$\vec{B} = \nabla s' \times \nabla\psi,$$

$$\psi = -u + \iota(s)v + \lambda(s,u,v),$$

$$\lambda(s_j,u,v) = \sum_m \sum_n \lambda_{jmn} \sin(2\pi(mu - nv)).$$

Here s' is the non-normalized flux. For each of the variables r, z, and λ there are M_U poloidal and $2M_V + 1$ toroidal modes, which are varied in VMEC to minimize the total energy and hence find the equilibrium. For this search the above expansions are evaluated on a mesh of N_U (poloidal direction) times N_V (toroidal direction) points. Of course one should observe $N_U \geq 3M_U$ and $N_V \geq 3M_V$. The search for the minimum is terminated when F_{SQ}, the square of the "force" (= derivative of the energy with respect to the Fourier coefficients), is less than a tolerance F_{TOL}. Another criterion for the quality of the minimization is provided by the quantity D_{ELBSQ}, which is essentially the difference in magnetic pressure in the vacuum and the plasma at the boundary. It should of course vanish for an exact solution.

The code package uses the VACUUM subroutine to compute the forces of the magnetic field on the plasma boundary. Since a call of this subroutine is computationally expensive, there is an option to call VACUUM only every N_{VAC} iteration steps.

To save computing time, an interpolation scheme has been introduced into the VACUUM subroutine. In the first call, $\vec{B}_0$ is computed by means of the Biot-Savart law on the mesh points of a mesh. In later calls, the time-consuming Biot-Savart integration is replaced by interpolation.

At the beginning of this project, only a VMEC version called CODE1510 was used. Later a new version called CODE7 became available. Since the convergence properties of the two versions turned out to be quite different, they are reported separately here.

2.1 CODE1510

All parameters introduced above were varied. The convergence is discussed on the basis of the resulting responses of the B_θ coils no. 1-6, which measure the poloidal magnetic field in the triangular cross-section, and "loop 3," which measures the magnetic flux through its surface.

Some results can be obtained from comparisons of single runs. Increasing N_{S} from 17 to 33 shows that this is not a critical parameter. Setting N_{U} much larger than $3M_{\mathrm{U}}$ has no effect. Analogously, increasing N_{V} too causes no big change either. Varying M_{V} from 8 to 12 has no drastic effect.

F_{TOL} is important and should therefore be lowered. However, the stopping criterion could not be satisfied within a reasonable time for too low values and the minimization was terminated after a number of iterations in some cases. Another important parameter is N_{VAC}. The best values are obtained if VACUUM is called in every iteration, but setting $N_{\mathrm{VAC}} = 1$ substantially increases the computing time.

To study the M_{U}-dependence, the responses of B_θ coil 1 and loop 3 were observed for increasing M_{U}. There is no convergence, certainly not below $M_{\mathrm{U}} = 12$.

The above results can be summarized by concluding that satisfactory convergence could not be achieved with the VMEC version CODE1510.

2.2 CODE7

The new "CODE7" version calls VACUUM in every iteration and is faster than the former one with $N_{\mathrm{VAC}} = 1$. The tolerance is set to the not readily attainable low value $F_{\mathrm{TOL}} = 10^{-13}$ and the iteration is stopped by setting an appropriate time limit (see below). Of course, $N_{\mathrm{U}} \geq 3M_{\mathrm{U}}$ and $N_{\mathrm{V}} \geq 3M_{\mathrm{V}}$ are observed as before. Regarding the F_{SQ} values achieved, it was found that they vary over several orders of magnitude without a corresponding variation in the diagnostic coil responses. Therefore, F_{SQ} provides no criterion for the accuracy of the responses. For such a criterion, D_{ELBSQ} is more appropriate. The lower values of D_{ELBSQ} belong to the higher values of M_{U} and M_{V} and scatter only within a 5% range, whereas the D_{ELBSQ} values above 10^{-3} belong to the lower values of M_{U} and M_{V} and deviate from the more accurate ones by roughly 10%. Therefore $D_{\mathrm{ELBSQ}} \approx 3 \times 10^{-4}$ has probably yielded the most accurate results. Concerning the convergence with M_{U} and M_{V}, the error exceeds 10% if any of these

parameters is set lower than 8. For 5% accuracy, $M_V = 10$ and $M_U = 12$ or $M_U = 14$ appear to be necessary. As for the convergence with N_S, no drastic dependence is found and $N_S \geq 33$ yields acceptable accuracy if M_U and M_V are not too low.

Finally, the convergence studies can be summarized in the following recommendations. To obtain 5% accuracy in the diagnostic coil responses and resolve the ripple of the modular coils, choose $M_U = 12$ or $M_U = 14$, $M_V = 10$, $N_U = 3M_U$, $N_V = 3M_V$, and $N_S = 41$, which require less than 2.7 Mwords, and iterate for 15,000 seconds on the Cray-XMP. If 10% accuracy is sufficient and the ripple does not need to be resolved, the specifications $M_U = M_V = 8$ and $N_S = 33$ will reduce the memory requirements below 1.8 Mwords in a 5,000 second run.

3 Diagnostic coil responses for two external fields

As a first contribution to a data bank the responses for two different external fields with zero longitudinal plasma current and a mass profile proportional to $(1-s)^2$ were computed and plotted versus β in Figs. 1 to 4. The first external field is the standard case (i.e. 37 kA in the modular field coils and no current in the toroidal and vertical field coils), which has a rotational transform of $\iota = 0.39$ at $\beta = 0$ and between $\iota = 0.46$ (axis) and $\iota = 0.37$ (boundary) at $\beta = 0.93\%$. The jobs were run with $M_U = 14$, $M_V = 10$, and $N_S = 41$. For the other case the currents are 33.987 kA in the modular, -20.879 kA in the toroidal and zero in the vertical field coils. This gives a rotational transform of $\iota = 0.5$ at $\beta = 0$ and of $\iota = 0.55$ (axis) and $\iota = 0.50$ (boundary), hence $\iota \approx 0.5$ overall, at $\beta = 0.95\%$. These jobs were run with $M_U = 12$, $M_V = 8$, and $N_S = 33$.

Figure 1 shows the responses of the B_θ coils no. 1-6, which are placed in the upper half of the triangular cross-section. Coils no. 7-12 in the lower half yield identical signals for symmetry reasons and need not be considered here. A comparison of the offset at $\beta = 0$ with Gardner's [1] results shows that the accuracy has been substantially improved.

Figure 2 shows the response of the "$\cos 2\theta$" coil, which measures the line integrals of the magnetic field due to the plasma current along each of four Rogowski coils (with alternating signs) positioned around a poloidal cross-section. Figures 3 and 4 show the responses of five loops which measure magnetic fluxes.

Poloidal cross-sections of the flux surfaces are shown in Figs. 5 and 6. In both cases the modular coil system entails a detailed structure in the plasma boundary. At the triangular cross-section, for example, there are nearly toroidally oriented parts of the coil system which produce the peculiar "clamped" behaviour of the flux surfaces. These details explain the high number of poloidal modes necessary for an accurate description.

4 Comparison with the "TRANS" data base

The data in TRANS are based on the results of the "KW" code, an ideal MHD equilibrium solver based on field line tracing. The vacuum fields are specified here by $\iota_{m+t,0}$, the rotational transform due to modular and toroidal field coils on the axis, and

$|B|_{\mathrm{m+t,0}}$, the modulus of the magnetic field due to these coils averaged over the axis. The pressure profile, of which only the height and width can be selected, is always bell-shaped and extends to infinity. This causes some problems when the TRANS data are compared with VMEC results. VMEC requires as input the currents in the field coils and an arbitrary mass profile which must vanish outside a finite effective plasma radius. During minimization the plasma is expanded or compressed and a pressure profile will result according to the law of adiabatic compression.

In a first test, the complications with the mass or pressure profile were avoided by comparing the vacuum field for the coil currents

$$I_{\mathrm{mod}} = 31.32\ \mathrm{kA}, \quad I_{\mathrm{tor}} = 4.08\ \mathrm{kA}, \quad I_{\mathrm{vert}} = 840\ \mathrm{A}.$$

Figure 7 shows very good agreement for the magnetic fields on the respective axes. The positions of these axes differ, however, by about 0.5 cm, as can be seen in Figs. 8 and 9. This might be tolerable but the disagreement in the rotational transform (Fig. 10) is not. It was later found that there was a small error in the representation of the modular coils [3].

For a comparison with plasma, $\iota_{\mathrm{m+t,0}} = 0.347$ and $B_{\mathrm{m+t,0}} = 2.537$ T are specified for the data base. These should correspond to the coil currents

$$I_{\mathrm{mod}} = 30.654\ \mathrm{kA}, \quad I_{\mathrm{tor}} = 10.299\ \mathrm{kA}, \quad I_{\mathrm{vert}} = 0.$$

The mass profile is proportional to

$$\rho(s) = 0.00398\{(1 + 2.6893s + 10.3578s^2)e^{-5.771s} - 0.043771\}.$$

The height and width of the pressure profile for the data base are chosen for approximate agreement with the VMEC result. This agreement and that of the rotational transform, which is much better than in the case before, is shown in Fig. 11. Figures 12 and 13 show that the positions of the axes and the effective radii also agree very well. Finally, the magnetic fields on the axes agree excellently (Fig. 14) except for a small constant shift, which could be corrected by a better choice of $B_{\mathrm{m+t,0}}$ without affecting the agreement of the other quantities.

To summarize, it can concluded that the agreement is generally good, provided that the same physical situation is accurately specified in the two different ways that the TRANS data base and the VMEC code require.

5 Preparative studies for the W7-AS data base

There are about 15 physical input parameters for a VMEC run:
the three currents in the external coils, i.e. in the modular, toroidal field and vertical field coils,
the plasma volume or, equivalently, the effective radius,
six coefficients of the mass-profile polynomial,
six coefficients of the ι-profile polynomial or five coefficients of the longitudinal plasma current profile.

A mesh with only three mesh points along each axis of this 15-dimensional parameter space would contain $3^{15} \approx 14 \times 10^6$ mesh points. Since the data base cannot contain so many cases, it must first be established what the relevant parameters are, i.e. on which the diagnostic signals sensitively depend. To this end, 24 runs of the VMEC/DIAGNO were performed with VMEC9011, a new version replacing CODE7. The computational parameters were, following Section 2: $N_S = 33$, $N_U = 40$, $N_V = 24$, $M_U = 10$, and $M_V = 8$. Concerning the physical parameters, the following sensitivities of the diagnostic signals were detected:

Coil currents: These contain only two relevant parameters, since a variation of all three currents would include an overall variation of the magnetic field. The relation of modular and toroidal field current determines the rotational transform of the vacuum field and this has already been shown to have a significant effect on the signals in Fig. 1. In Fig. 15, the signals are plotted versus the vertical field current I_{vert}. At the highest I_{vert} shown, the B_z field is 1.4% of B_0 and some signals have changed by up to 50%. Thus, I_{vert} is certainly a relevant parameter too.

$\langle\beta\rangle$: The sensitivity has also been shown in Fig. 1.

Mass or pressure profile at fixed $\langle\beta\rangle$ and fixed effective radius: That the signals are not very sensitive to the normalized profiles has already been shown by Gardner [1]. It was found that this even holds for a very broad profile $\sim 1 - s^5$.

Effective radius or volume V: Figure 16 shows that the signals strongly depend on this parameter. The dependence on $\langle\beta\rangle$ and V is such that only variations of their product produce significant variations in the signals. The identity $\langle\beta\rangle V = \int \beta \mathrm{d}V$ shows that this is only another manifestation of the insensitivity with respect to normalized profiles.

Longitudinal plasma current: Figure 17 shows that the dependence of the signals on the total longitudinal current is linear even though various profiles were used. Two runs with 15 kA showed that the linearity even extends to this high current.Only for two unusual profiles with 12 kA near the axis in one direction and 12 kA near the boundary in the opposite direction does a deviation from linearity occur. It must be concluded therefrom that changes in the current profile have to be drastic to be detectable in the diagnostic signals. Near-linearity was also found for $\iota \approx 0.5$ (Fig. 18) and for lower $\langle\beta\rangle$ (Fig. 19).

6 W7-AS data base and diagnostic signal inversion

On the basis of the preceding section, the essential dependence of the diagnostic signals on various physical parameters can now be summarized. The signals are sensitive to a change in:

(1) the external field, which is determined by three currents of which two can be varied,
(2) the total longitudinal current J_{tor}
(3) and the product $\langle\beta\rangle V$, which includes the dependence on the effective plasma radius.

On this basis, an equilibrium data base for W7-AS was obtained with 36 equilibria and $\iota \approx 1/3$. The following parameters were systematically varied: $J_{\text{tor}} = -5$ kA, 0, +5 kA; $\beta = 0$, 0.005, 0.01; effective radius = 11.5 cm, 18 cm;

$B_z = 0$, 0.02 T (inward shift). The runs are listed in Tables 1 and 2.

To interpolate the data base to arbitrary values of $J_{\rm tor}$ and $\langle\beta\rangle V$, every diagnostic signal Y_i is assumed to be the sum of two independent terms, one linear in $J_{\rm tor}$ and one slightly nonlinear (see Fig. 1) in $\langle\beta\rangle V$:

$$Y_i = a_i J_{\rm tor} + b_i \mathrm{arcsinh}(c\langle\beta\rangle V). \qquad (1)$$

The parameters a_i, b_i and c are determined by a least squares fit where the differences were weighted by multiplying them with a scale factor, see Tables 1 and 2.

Since all currents, including $J_{\rm tor}$, can easily be measured in the experiment, the only variable that remains to be determined from the diagnostic signals is $\langle\beta\rangle V$. Inversion of (1) yields

$$\langle\beta\rangle V = \frac{1}{c}\sinh\left(\frac{Y_i - a_i J_{\rm tor}}{b_i}\right). \qquad (2)$$

The right-hand side of (2) thus provides the estimate of $\langle\beta\rangle V$ derived from Y_i. The deviation of this estimate from the actual value is listed in Tables 3 and 4 as root mean square deviation and indicates which signals might provide reliable estimates.

One finds for Tables 1 and 3 that signals no. 1, 4, 5, 6, 7, 9, and 10 reproduce the correct value within less than 5% of the largest value (0.0127 m^3) and that all except no. 3, 8, and 11 remain within the 10% limit. For Tables 2 and 4 signals no. 2, 7, 8, and 10 reproduce the correct value within 5.2% of the largest value (0.00639 m^3) or better, and all except no. 3, 4, and 11 are better than 10%.

This result is, however, not yet proof of reliability, since the interpolation reproduced only the data to which the parameters were fitted. A more stringent test is the derivation of $\langle\beta\rangle V$ from diagnostic signals of an extra VMEC run which was not involved in the fitting process. Such a case is shown in Table 5 for the data in Tables 1 and 3. The results from signals no. 5, 7, 8, 9, and 10 are near or within the 10% range and nos. 3, 6, and 11 do not yield reliable results. For the data in Tables 2 and 4 the situation is similar (see Table 6). Except for no. 11, the accuracy is near 10% or better, showing the consistency of the method, but now nos. 1, 5, 7, 8, and 9 are the best. To derive $\langle\beta\rangle V$ from given signals, it is therefore recommended to take the average from nos. 1, 2, 5, 7, 9, and 10, and assume an error of 5 to 10%.

The total error of the present diagnostic concept is composed of the following contributions:

1. limitations in computing power, i.e. finite values of computational parameters ($M_{\rm U}$, $M_{\rm V}$, $N_{\rm U}$, $N_{\rm V}$, $N_{\rm S}$) and computing time: 5 to 10%,
2. neglect of the small influence of profiles: 5%,
3. non-perfect interpolation of the signals: 5 to 10%,
4. the experimental error in the signals: 10% [4].

Since these contributions are probably independent, the total error in $\langle\beta\rangle V$ should be around 15%. It should be mentioned in this context that a discrepancy between Gardner's values [1] and the experimental ones has now been resolved [4] and that the agreement is now within 10%.

Acknowledgements

The author thanks P. Merkel for his guidance. He is also grateful to H. Maaßberg and F. Sardei for their cooperation in the comparisons with the data base and to J. Nührenberg for advice in several cases.

References

[1] H.J. Gardner, Nuclear Fusion **30** (1990) 1417-1424.
[2] S.P. Hirshman and O. Betancourt, J. Comput. Phys. **96** (1991) 99.
[3] P. Merkel, private communication.
[4] H. Renner, private communication.

Tables

Table 1: Job numbers 'EJRnnn' and craylist-file names 'DABAmmm' of the data base for modular coil current 29.9 kA, toridal field current 15.5 kA and zero vertical field ($\iota \approx 1/3$).

DABA...	EJR...	r_{eff}/cm	$\langle\beta\rangle$/%	J_{tor}/kA
001	655	18.0	0.0	0
002	656	18.0	0.5	0
003	657	18.0	1.0	0
004	702	11.5	0.0	0
005	703	11.5	0.0	5
006	704	11.5	0.0	-5
007	706	11.5	0.5	0
008	707	11.5	0.5	5
009	708	11.5	0.5	-5
010	709	11.5	1.0	0
011	710	11.5	1.0	5
012	711	11.5	1.0	-5
013	669	18.0	0.0	5
014	670	18.0	0.0	-5
015	671	18.0	0.5	0
016	672	18.0	0.5	-5
017	673	18.0	1.0	5
018	675	18.0	1.0	-5

Table 2: Job numbers 'EJRnnn' and craylist-file names 'DABAmmm' of the data base for modular coil current 30.1 kA, toroidal field current 7.8 kA, and vertical field current 0.84 kA ($\iota \approx 1/3$, $B_z = 0.02$ T).

DABA...	EJR...	r_{eff}/cm	$\langle\beta\rangle$/%	J_{tor}/kA
021	676	18.0	0.0	0
022	677	18.0	0.0	5
023	678	18.0	0.0	-5
024	684	18.0	0.5	0
025	683	18.0	0.5	5
026	682	18.0	0.5	-5
027	685	18.0	1.0	0
028	686	18.0	1.0	5
029	687	18.0	1.0	-5
030	713	11.5	0.0	0
031	714	11.5	0.0	5
032	715	11.5	0.0	-5
033	716	11.5	0.5	0
034	717	11.5	0.5	5
035	718	11.5	0.5	-5
036	719	11.5	1.0	0
037	720	11.5	1.0	5
038	721	11.5	1.0	-5

Table 3: Parameters for the interpolation formula determined from the data in Table 1 by a least squares fit with scaled differences. $c = 90$ m^{-3}. Insert J_{tor} in amperes to obtain Y_i in correct units. 'r.m.s.' is the root mean square deviation between $\langle\beta\rangle V$ and the value from the inversion formula. The largest value of $\langle\beta\rangle V$ is 0.0127 m^3.

i	a_i	b_i	scale factor	unit of Y_i	r.m.s./10^{-6}m^3
1	-4.106E-7	-1.277E-2	100	T	548
2	-3.062E-7	-4.410E-3	100	T	802
3	-2.911E-7	-1.344E-4	100	T	35900
4	-3.587E-7	2.316E-3	100	T	583
5	-4.967E-7	5.659E-3	100	T	581
6	-5.217E-7	7.062E-3	100	T	569
7	2.622E-8	1.735E-3	300	Wb	459
8	4.691E-8	1.963E-3	300	Wb	1370
9	3.116E-8	1.260E-3	300	Wb	551
10	3.023E-6	2.808E-2	30	Wb	300
11	2.326E-6	-1.397E-2	30	Wb	2250

Table 4: Parameters for the interpolation formula determined from the data in Table 2 by a least squares fit with scaled differences. $c = 77$ m^{-3}. Insert J_{tor} in amperes to obtain Y_i in correct units. 'r.m.s.' is the root mean square deviation between $\langle\beta\rangle V$ and the value from the inversion formula. The largest value of $\langle\beta\rangle V$ is 0.00639 m^3.

i	a_i	b_i	scale factor	unit of Y_i	r.m.s./10^{-6}m^3
1	-3.692E-7	-1.309E-2	100	T	423
2	-3.099E-7	-6.310E-3	100	T	290
3	-2.857E-7	-1.637E-3	100	T	11800
4	-3.643E-7	2.101E-3	100	T	7510
5	-5.667E-7	7.523E-3	100	T	495
6	-6.018E-7	1.071E-2	100	T	533
7	1.964E-8	1.887E-3	300	Wb	335
8	2.077E-8	2.552E-3	300	Wb	258
9	2.558E-8	1.579E-3	300	Wb	373
10	2.996E-6	3.250E-2	30	Wb	248
11	2.039E-6	-1.848E-2	30	Wb	5590

Table 5: $(\langle\beta\rangle V)_i$ values from diagnostic signals Y_i of a VMEC run. The coil currents are as in Table 1 and $\langle\beta\rangle = 0.00308$, $V = 1.297793$ m^3, and $J_{\text{tor}} = 6841$ A were chosen arbitrarily. $\langle\beta\rangle V = 0.003997$ m^3, Job EJR734, File DABA019.

i	$(\langle\beta\rangle V)_i/10^{-6}\text{m}^3$
1	3450
2	4810
3	58700
4	2730
5	4020
6	5120
7	3580
8	3560
9	4210
10	3710
11	3320

Table 6: $(\langle\beta\rangle V)_i$ values from diagnostic signals Y_i of a VMEC run. The coil currents are as in Table 2 and $\langle\beta\rangle = 0.00644$, $V = 0.524200$ m^3 and $J_{\text{tor}} = 1319$ A were chosen arbitrarily. $\langle\beta\rangle V = 0.003376$ m^3, Job EJR725, File DABA040.

i	$(\langle\beta\rangle V)_i/10^{-6}\text{m}^3$
1	3360
2	3710
3	3000
4	3200
5	3360
6	3490
7	3310
8	3370
9	3390
10	3590
11	2690

Captions

Fig. 1: Responses of the B_θ coils no. 1-6. Left: standard case; right: $\iota \approx 0.5$.

Fig. 2: Response of the $\cos 2\theta$ coil. Left: standard case; right: $\iota \approx 0.5$.

Fig. 3: Response of the inner (○) and outer (□) midplane loops. Left: standard case; right: $\iota \approx 0.5$.

Fig. 4: Response of loop 1 (○), loop 2 (□) and loop 3 (+). Left: standard case; right: $\iota \approx 0.5$.

Fig. 5: Flux surfaces for the standard case at $\beta = 0.934\%$ for poloidal cross-sections at $\phi = 36°$, $54°$, and $72°$.

Fig. 6: Flux surfaces for $\iota \approx 0.5$ at $\beta = 0.945\%$ for poloidal cross-sections at $\phi = 36°$, $54°$, and $72°$.

Fig. 7: Magnetic field on axis. Top: TRANS data base; bottom: VMEC result.

Fig. 8: Effective radius of flux surfaces versus their intersection with the x-axis. Left: TRANS; right: VMEC.

Fig. 9: Effective radius of flux surfaces versus their intersection with a radial line at $z = 0$ and $\phi = 36°$. Left: TRANS; right: VMEC.

Fig. 10: Rotational transform versus effective radius. Left: TRANS; right: VMEC.

Fig. 11: Rotational transform versus effective radius. Left: TRANS; right: VMEC.

Fig. 12: Effective radius of flux surfaces versus their intersection with the x-axis. Dashed line for vacuum field. Left: TRANS; right: VMEC.

Fig. 13: Effective radius of flux surfaces versus their intersection with a radial line at $z = 0$ and $\phi = 36°$. Dashed line for vacuum field. Left: TRANS; right: VMEC.

Fig. 14: Magnetic field on the axis. Top: TRANS data base; bottom: VMEC result.

Fig. 15: Diagnostic signals versus the current in the vertical field coils for the standard case and $\langle\beta\rangle = 0.0092$. At the highest current shown, $B_z = 0.014 B_0$ (inward shift).
Left: ○, □, +, △, ×, ◇; B_θ coils 1-6 respectively, i.e. from bottom to top.
Centre: ○, □, +; loop 2, loop 3, loop 1′.
Right: ○, □; outer and inner midplane loops.

Fig. 16: Diagnostic signals versus effective radius for the standard case and $\langle\beta\rangle = 0.0091$. One value of the B_θ coil 1 is out of place because this coil is inside the plasma in this case. Symbols as in Fig. 15.

Fig. 17: Diagnostic signals versus total longitudinal plasma current for the standard case at $\langle\beta\rangle = 0.0091$. Symbols as in Fig. 15.

Fig. 18: Diagnostic signals versus total longitudinal plasma current for $\iota = 0.5$ and $\langle\beta\rangle = 0.0091$. Symbols as in Fig. 15.

Fig. 19: Diagnostic signals versus total longitudinal plasma current for $\iota = 0.5$ (broken line) and standard case (full line) at $\langle\beta\rangle = 0.0091$. Symbols as in Fig. 15.

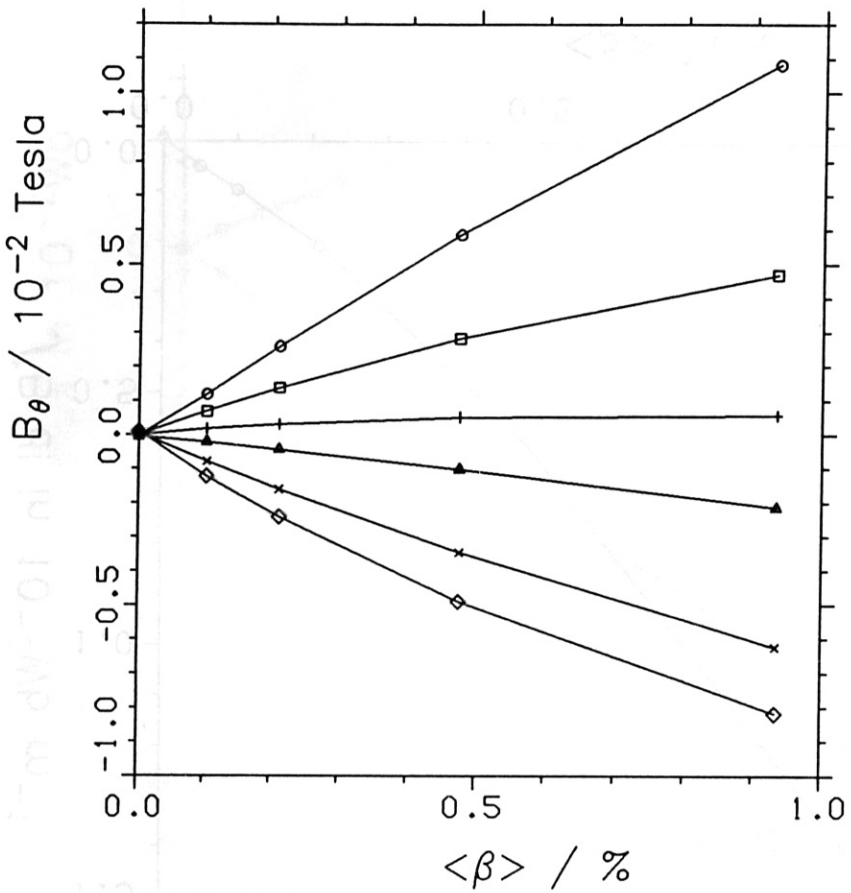
B_θ / 10^{-2} Tesla
1.0
0.5
0.0
-0.5
-1.0
0.0
0.5
1.0
<β> / %

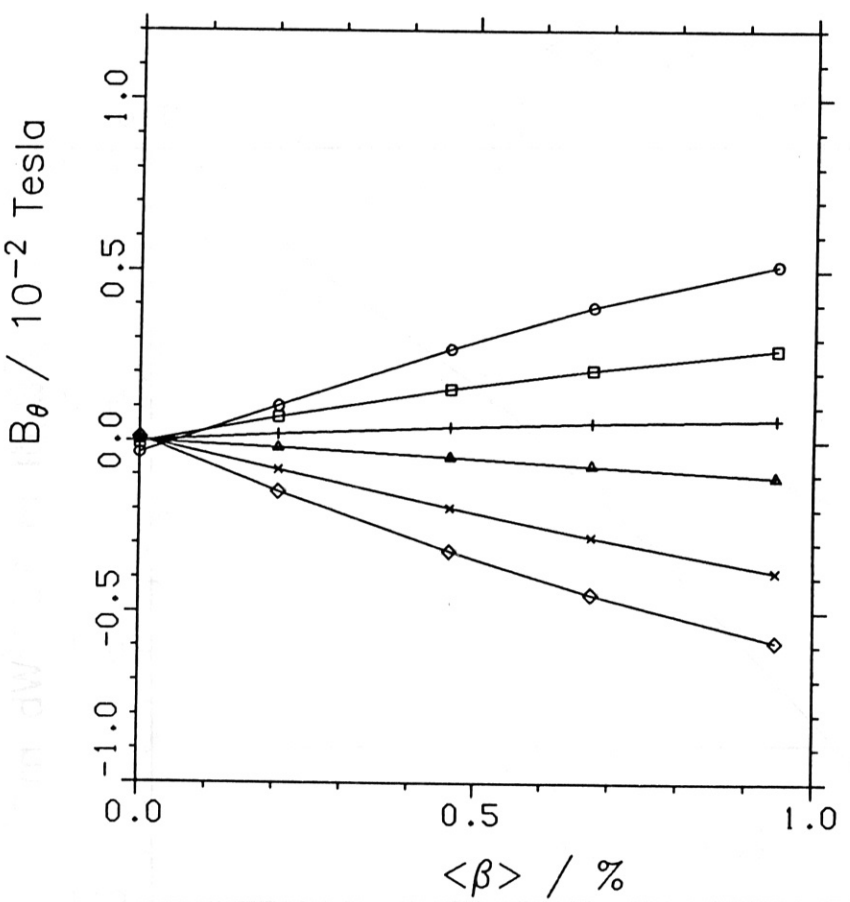
B_θ / 10^{-2} Tesla
1.0
0.5
0.0
-0.5
-1.0
0.0
0.5
1.0
<β> / %

FIG. 1

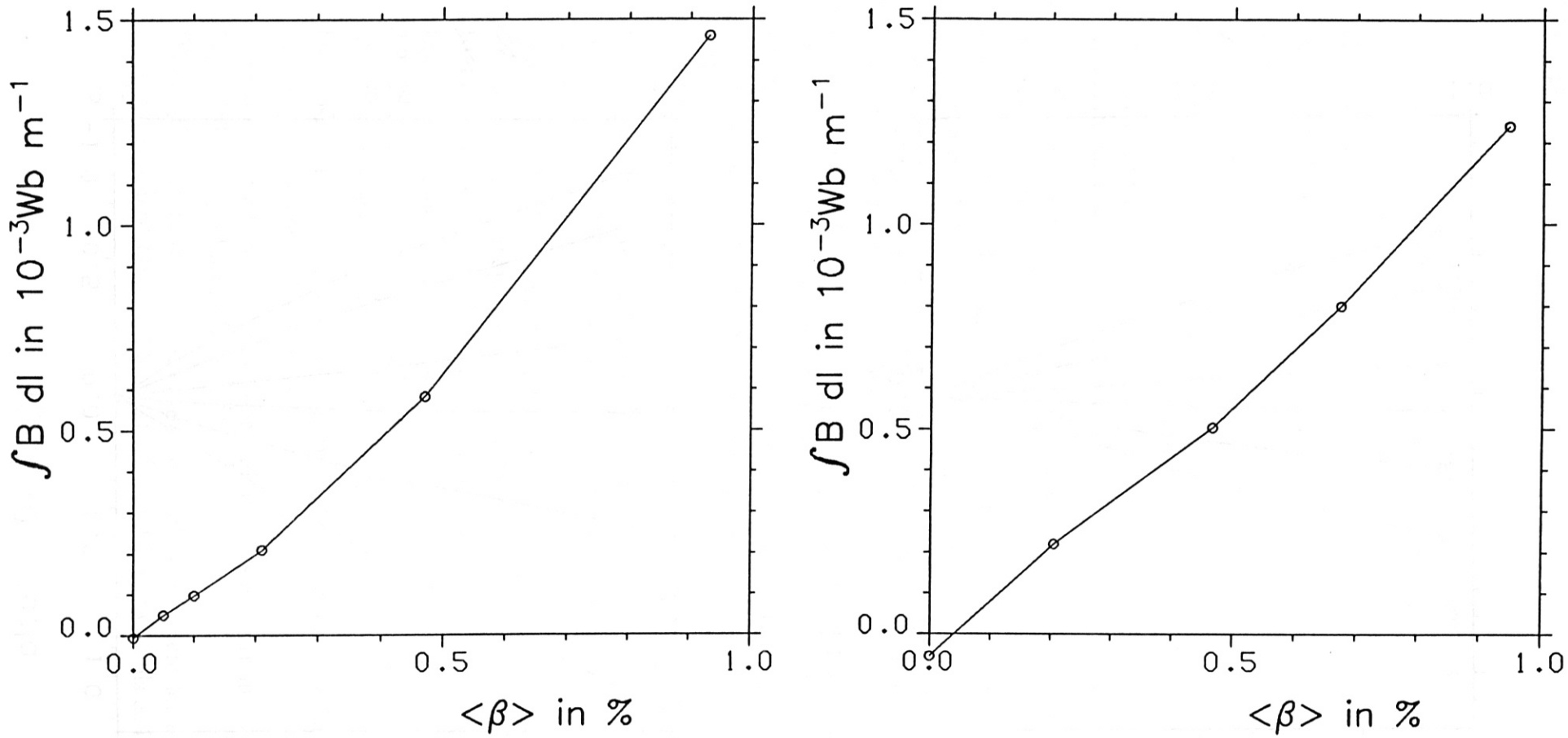
1.5
1.0
0.5
0.0
0.0
0.5
1.0
$\int B\,dl$ in 10^{-3}Wb m^{-1}
$<\beta>$ in %
1.5
1.0
0.5
0.0
0.0
0.5
1.0
$\int B\,dl$ in 10^{-3}Wb m^{-1}
$<\beta>$ in %

FIG. 2

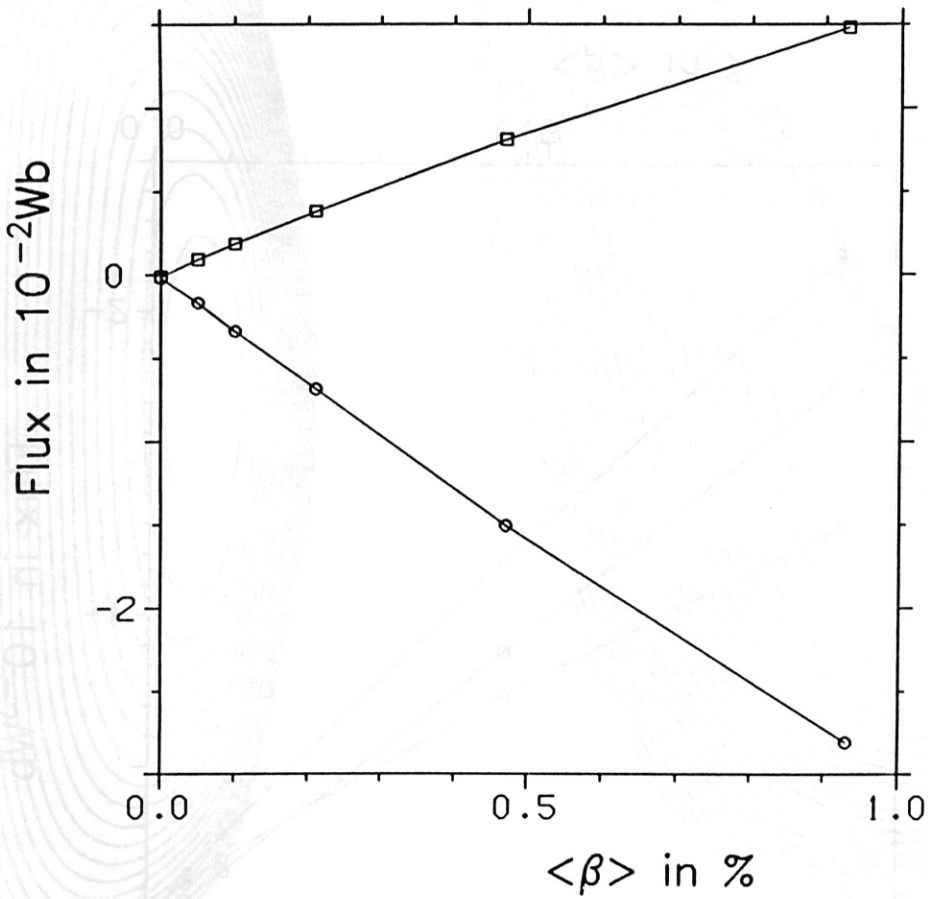

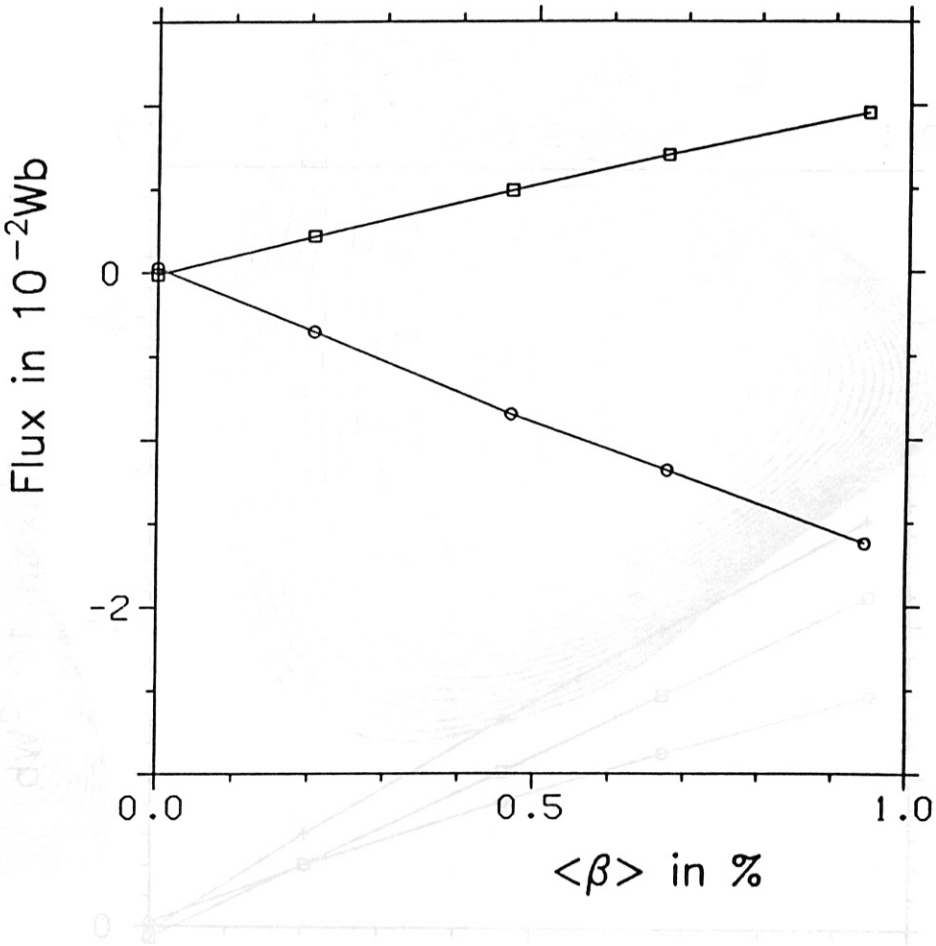

FIG. 3

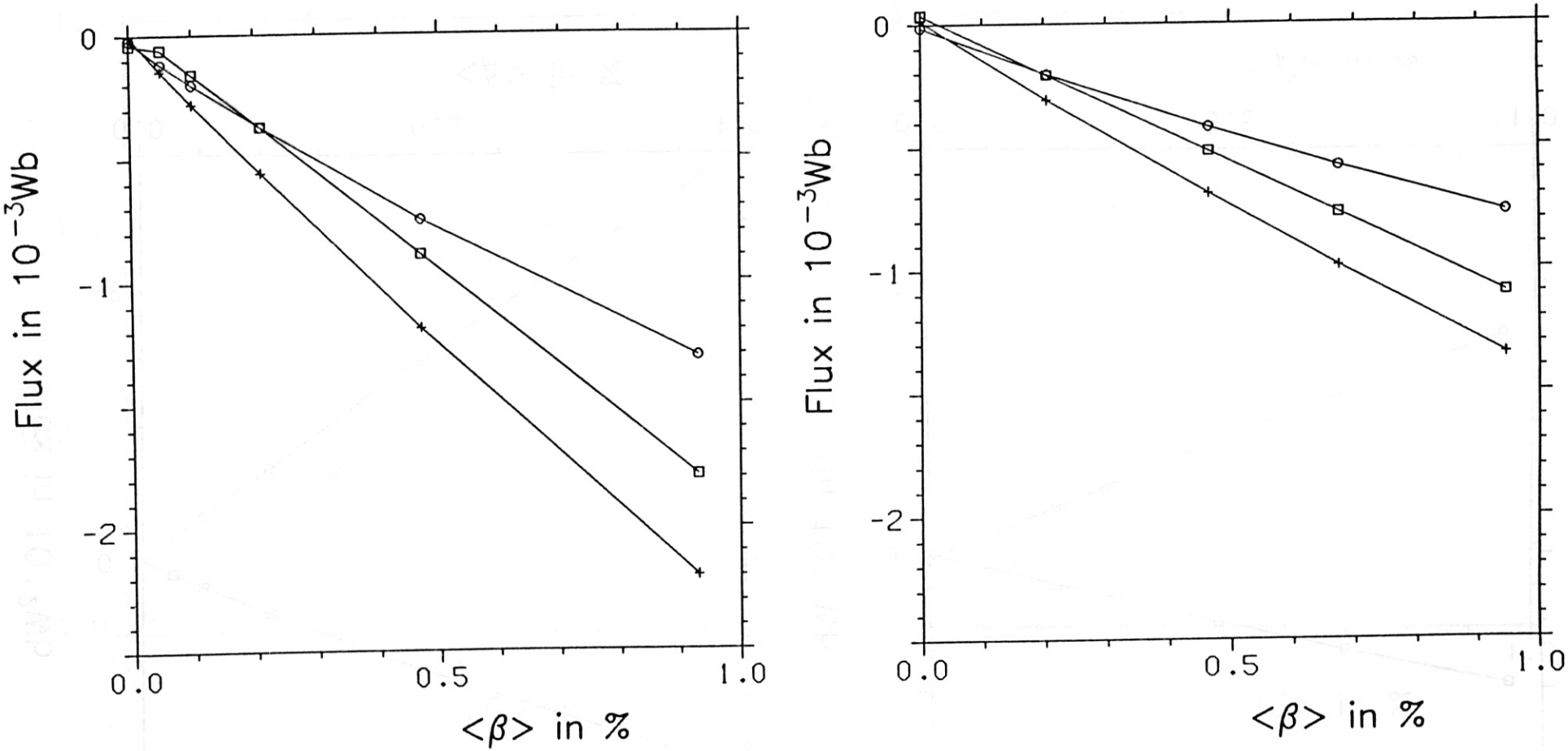

FIG. 4

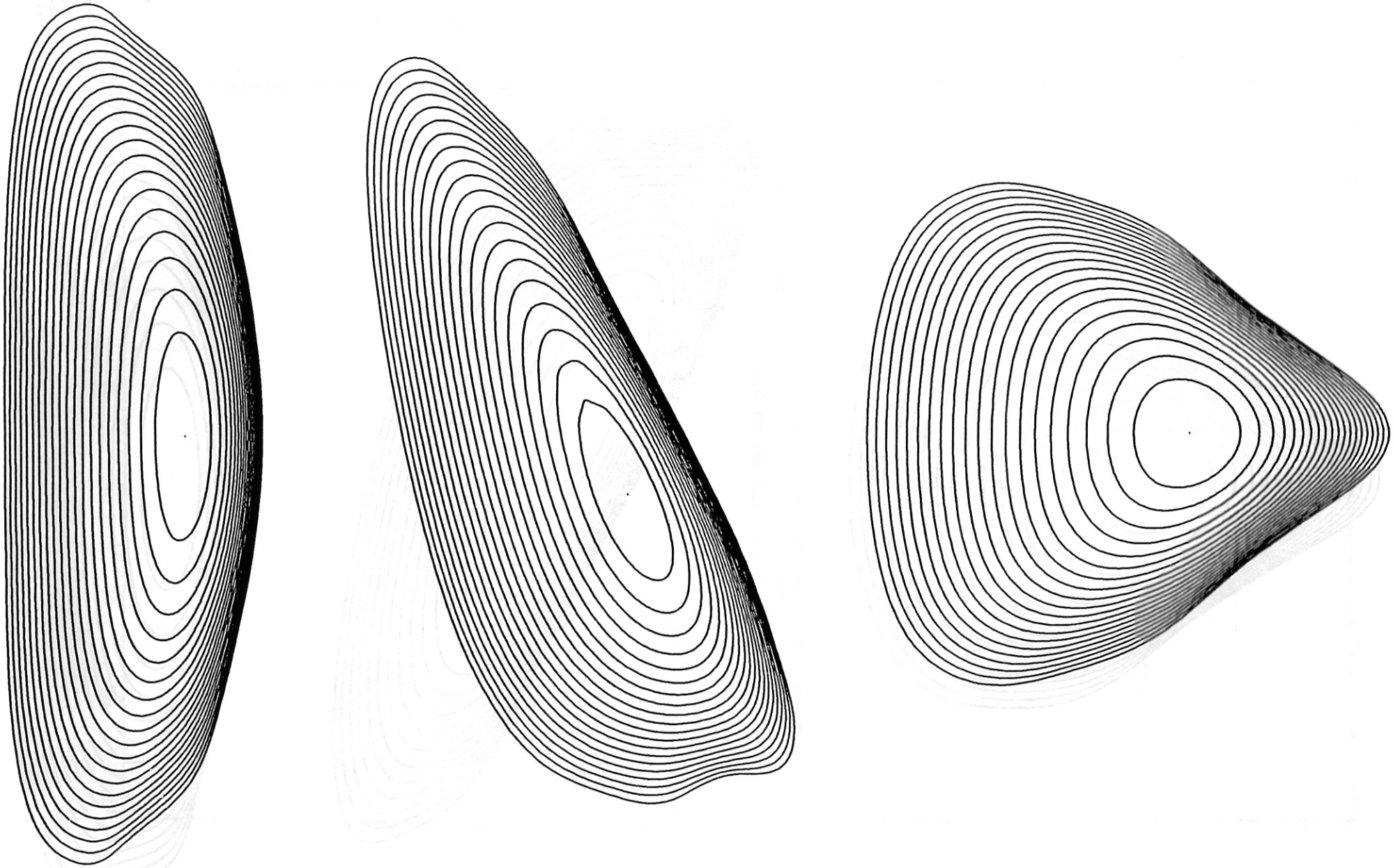

FIG. 5

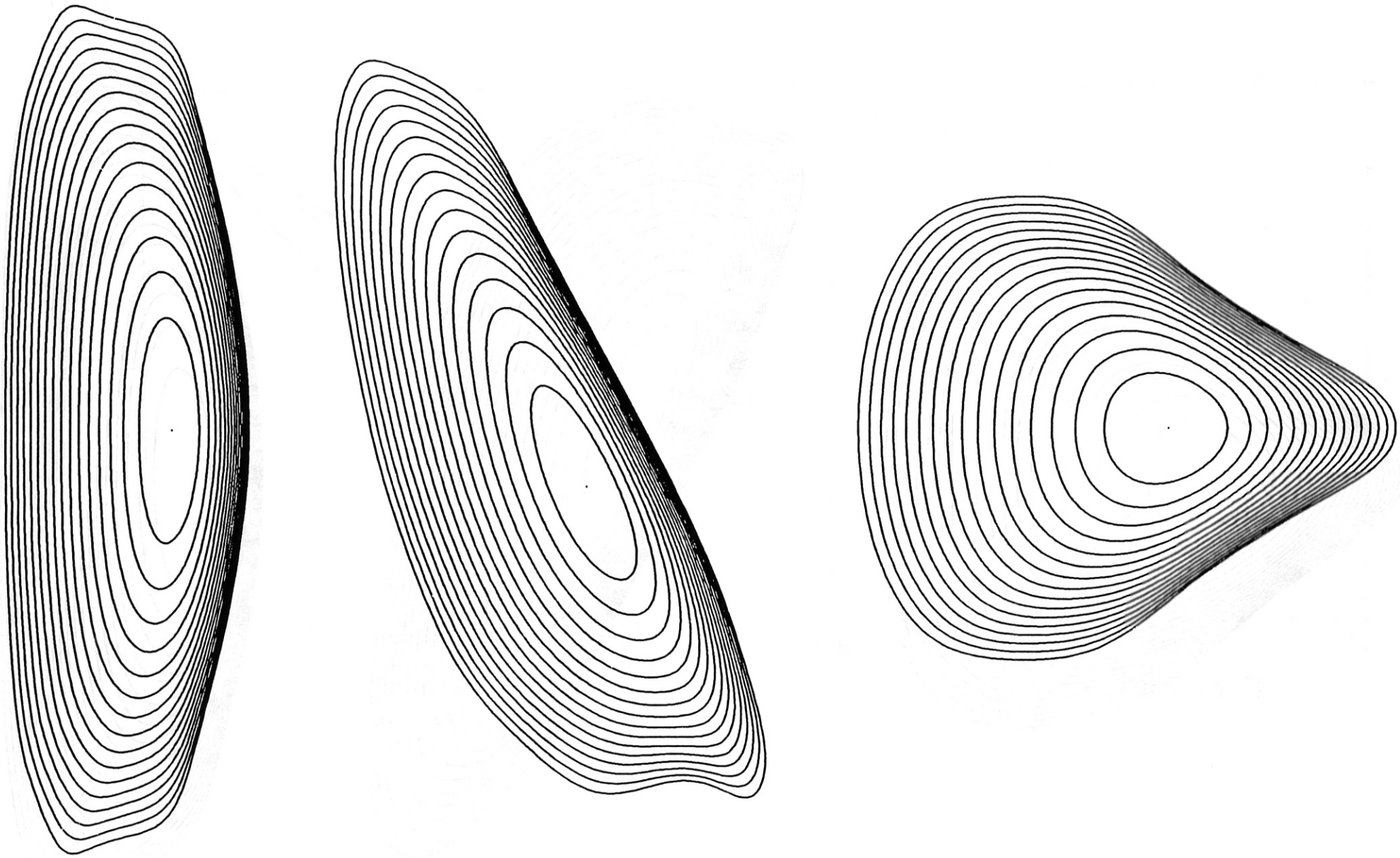

FIG. 6

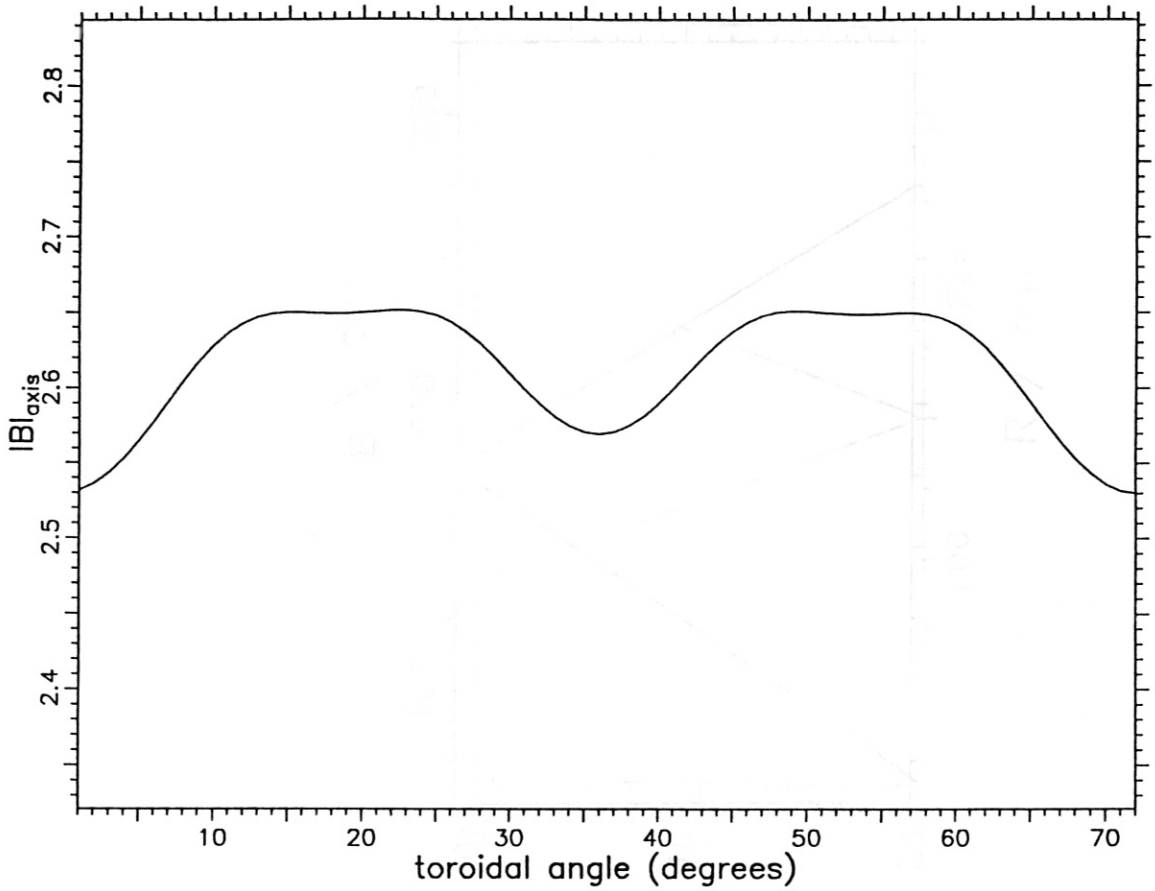
$|B|_{axis}$
2.8
2.7
2.6
2.5
2.4
10
20
30
40
50
60
70
toroidal angle (degrees)

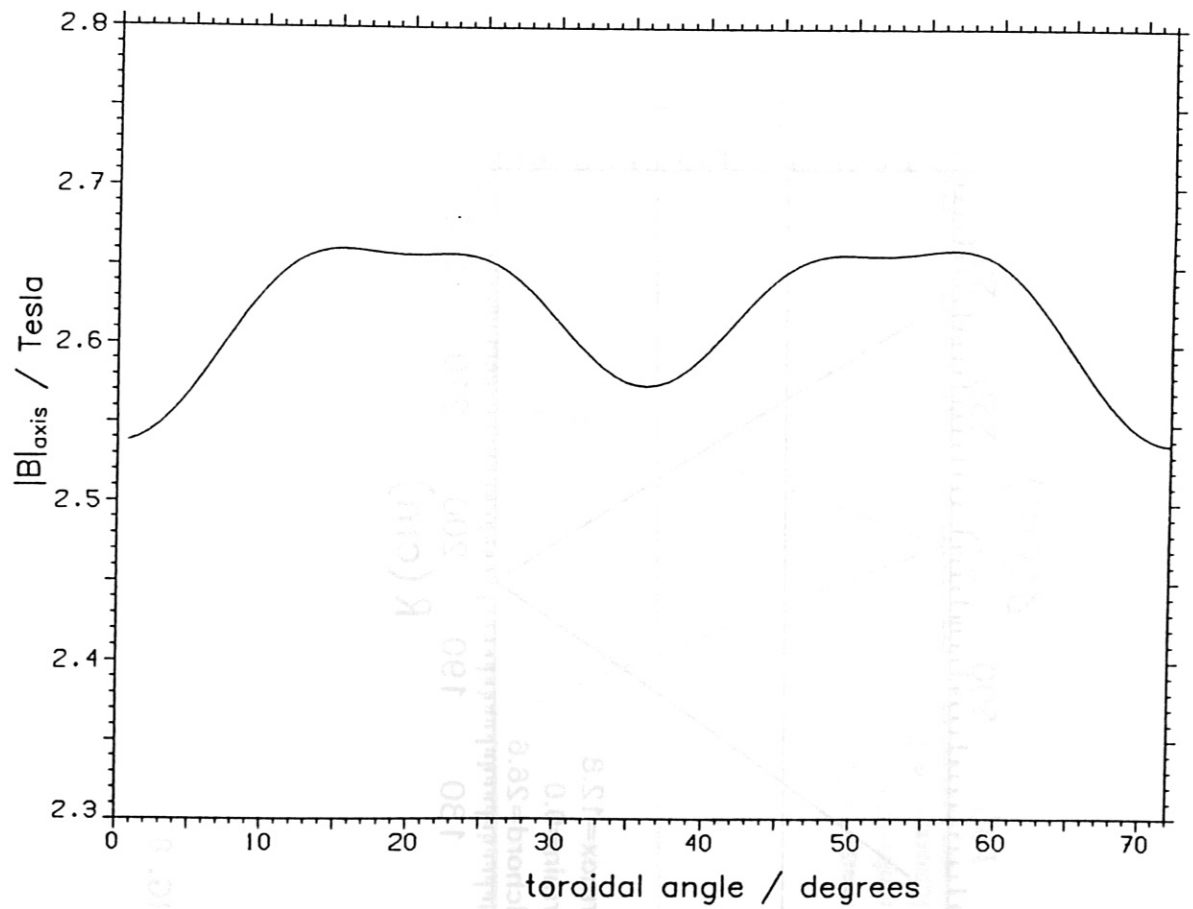
$|B|_{axis}$ / Tesla
2.8
2.7
2.6
2.5
2.4
2.3
0
10
20
30
40
50
60
70
toroidal angle / degrees

FIG. 7

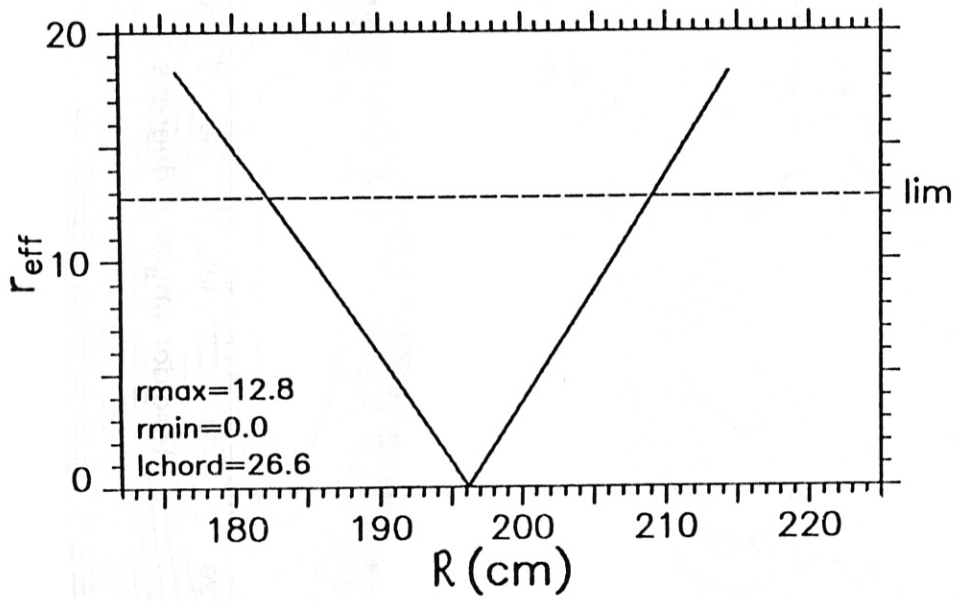
20
10
0
r_{eff}
lim
rmax=12.8
rmin=0.0
lchord=26.6
180
190
200
210
220
R (cm)

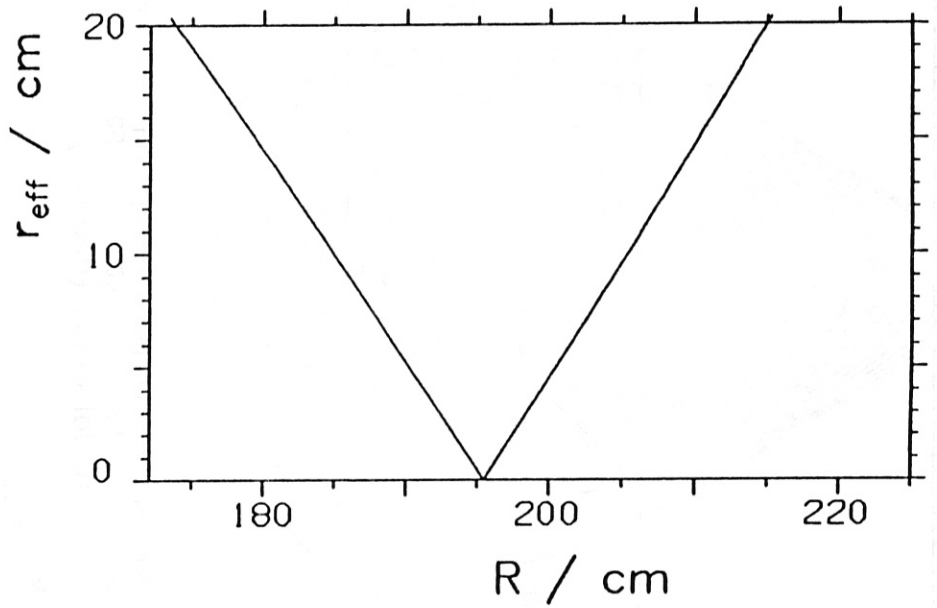
20
10
0
r_{eff} / cm
180
200
220
R / cm

FIG. 8

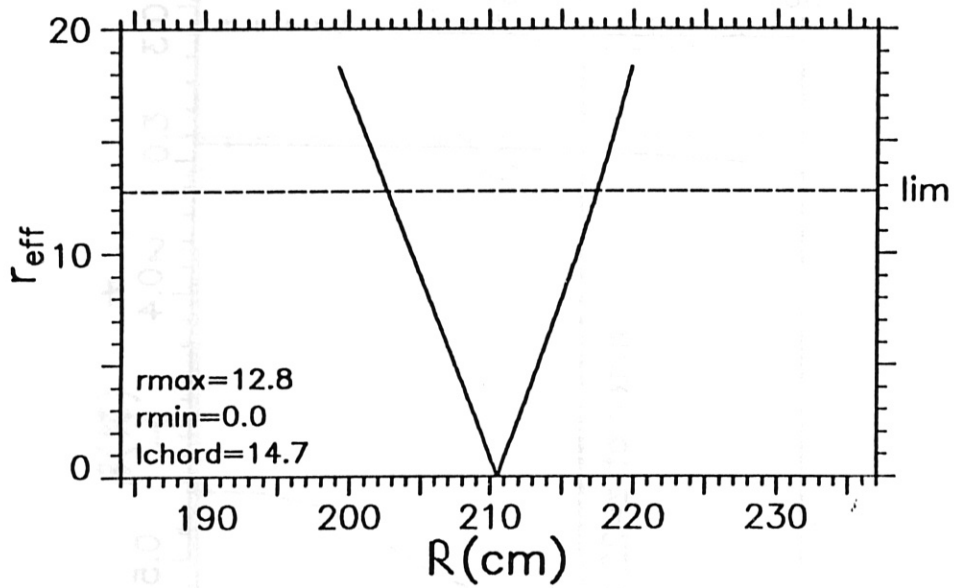
20
10
0
r_{eff}
lim
rmax=12.8
rmin=0.0
lchord=14.7
190
200
210
220
230
R(cm)

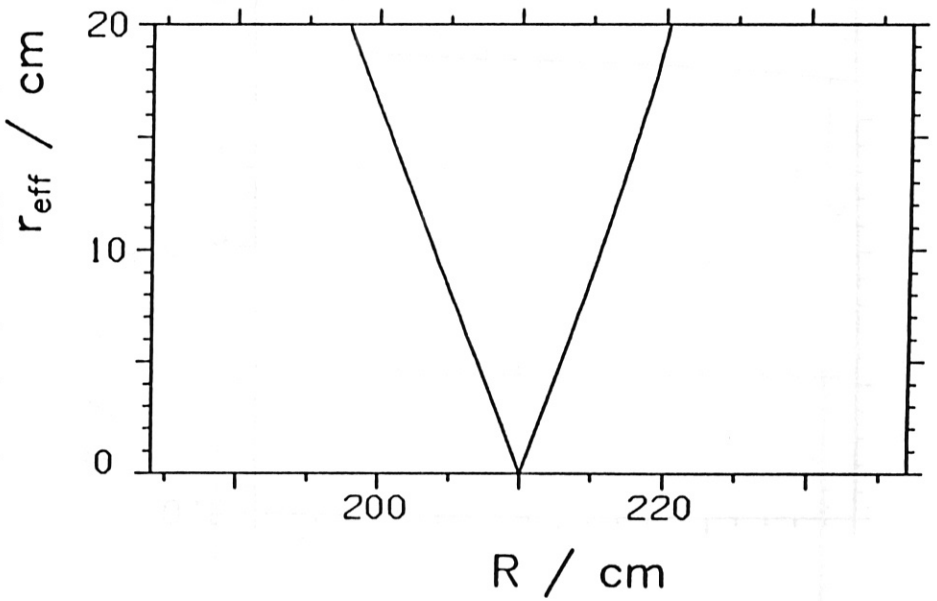
20
10
0
r_{eff} / cm
200
220
R / cm

FIG. 9

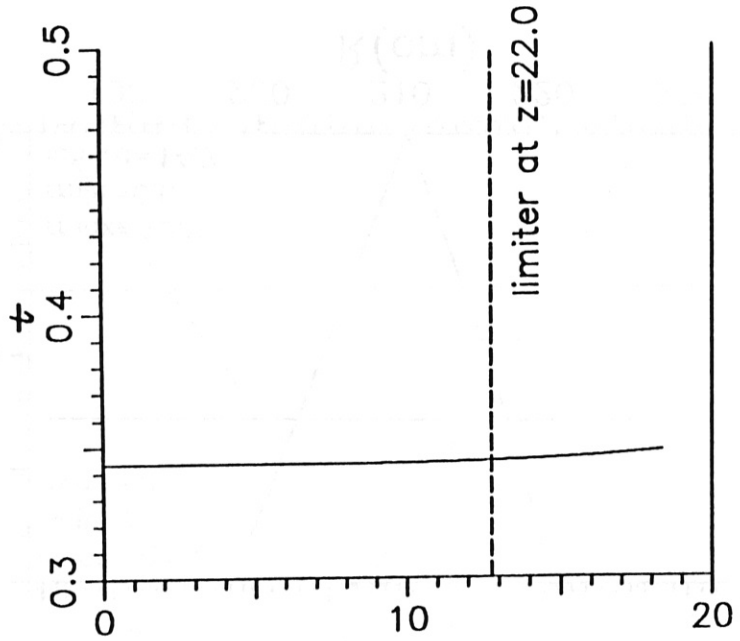

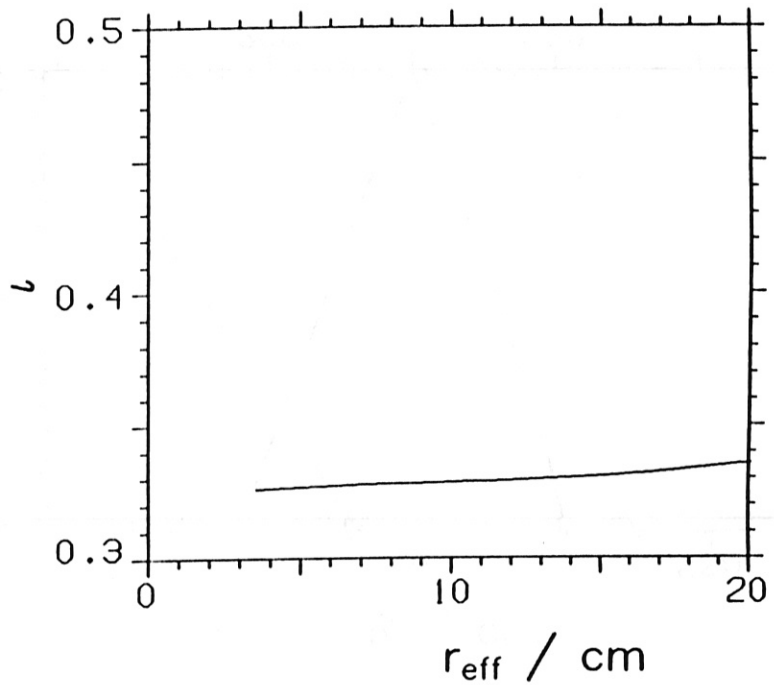

FIG. 10

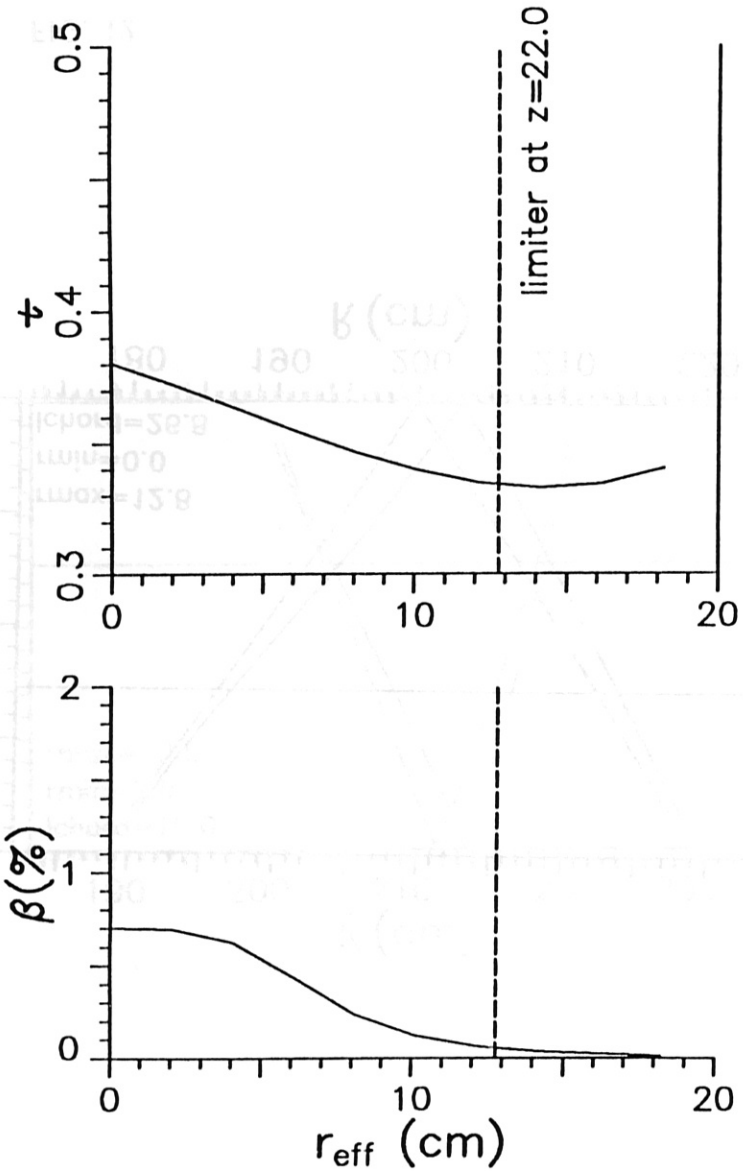
limiter at z=22.0
ι
0.5
0.4
0.3
0
10
20
β(%)
2
1
0
0
10
20
r_eff (cm)

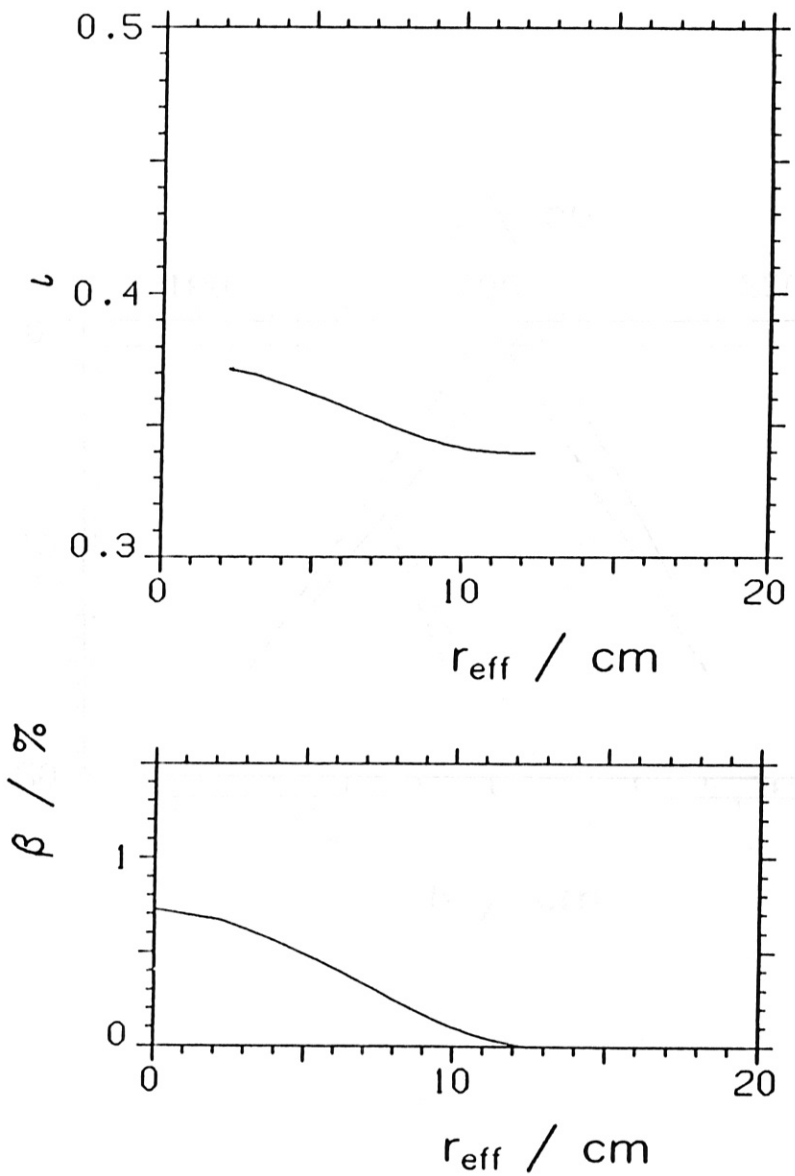
ι
0.5
0.4
0.3
0
10
20
r_eff / cm
β / %
1
0
0
10
20
r_eff / cm

FIG. 11

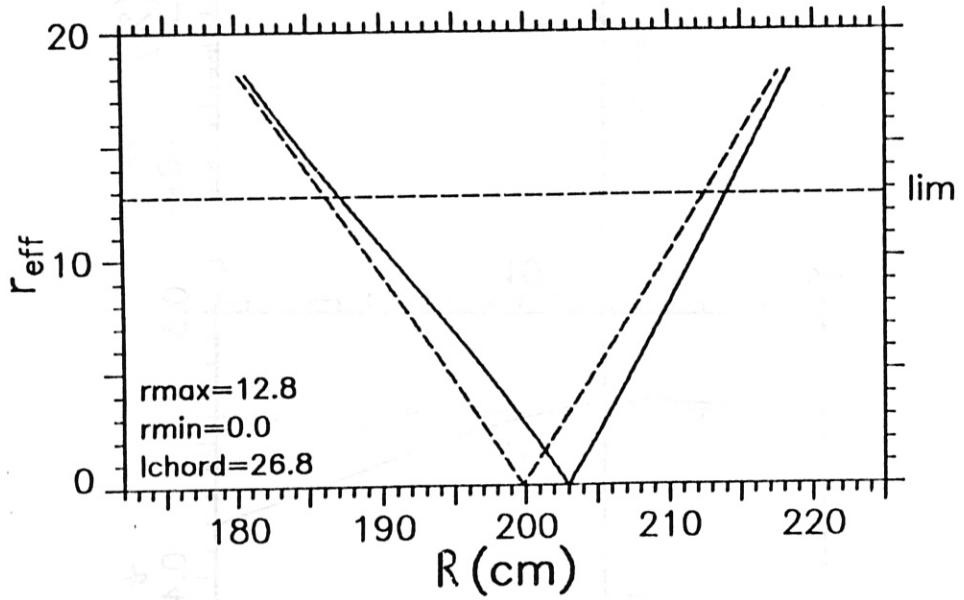
20
10
0
r_{eff}
lim
rmax=12.8
rmin=0.0
lchord=26.8
180
190
200
210
220
R (cm)

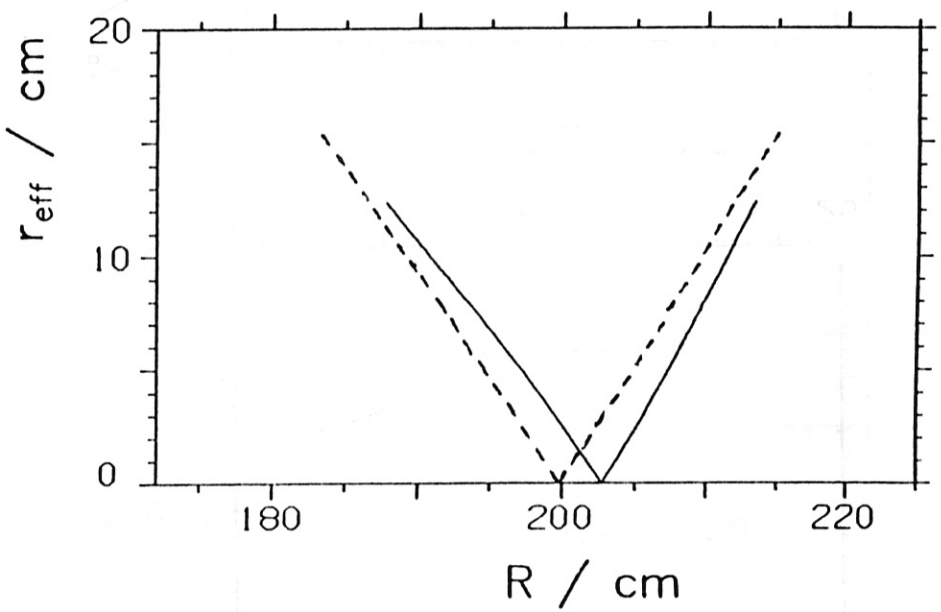
20
10
0
r_{eff} / cm
180
200
220
R / cm

FIG. 12

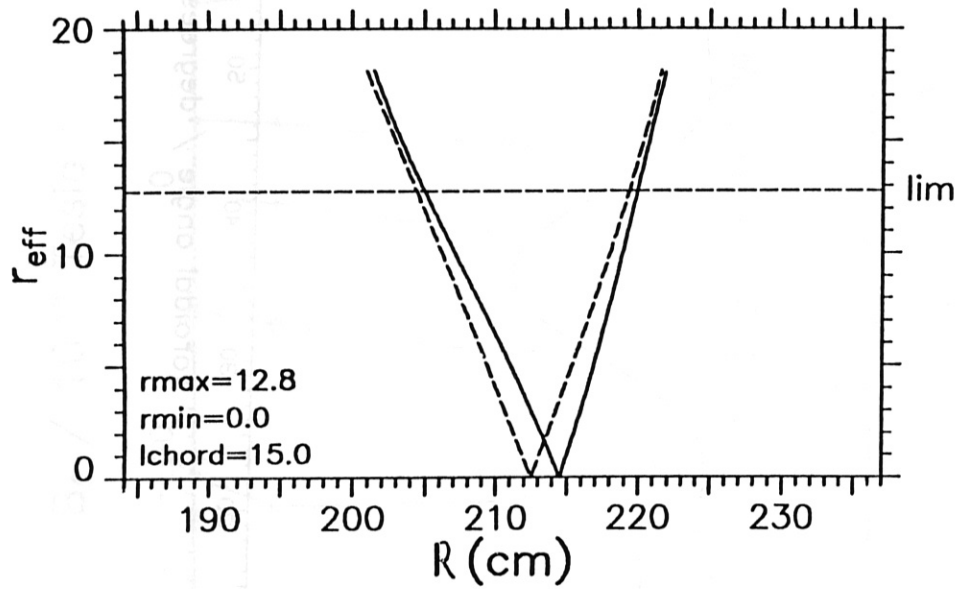
20
10
0
r_{eff}
lim
rmax=12.8
rmin=0.0
lchord=15.0
190
200
210
220
230
R (cm)

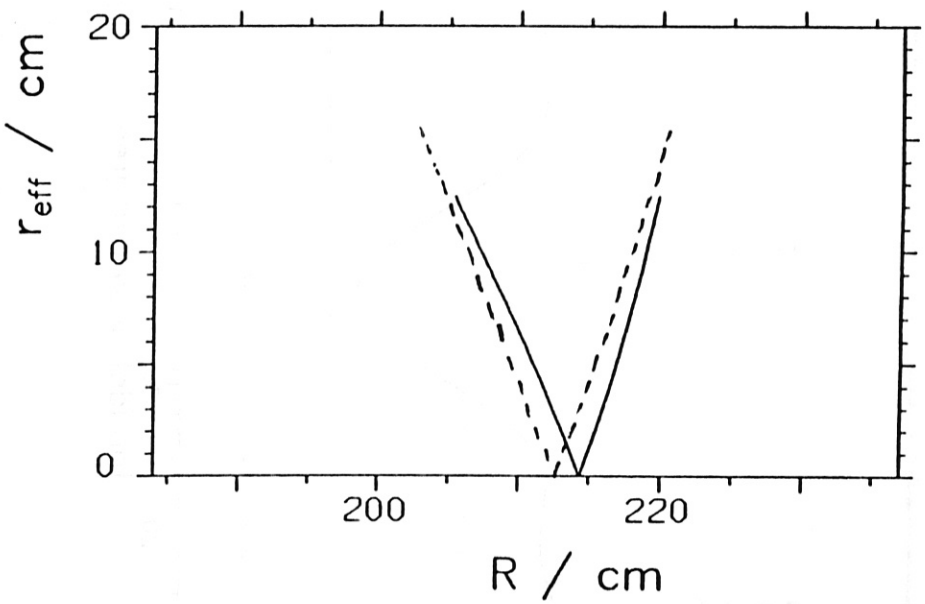
20
10
0
r_{eff} / cm
200
220
R / cm

FIG. 13

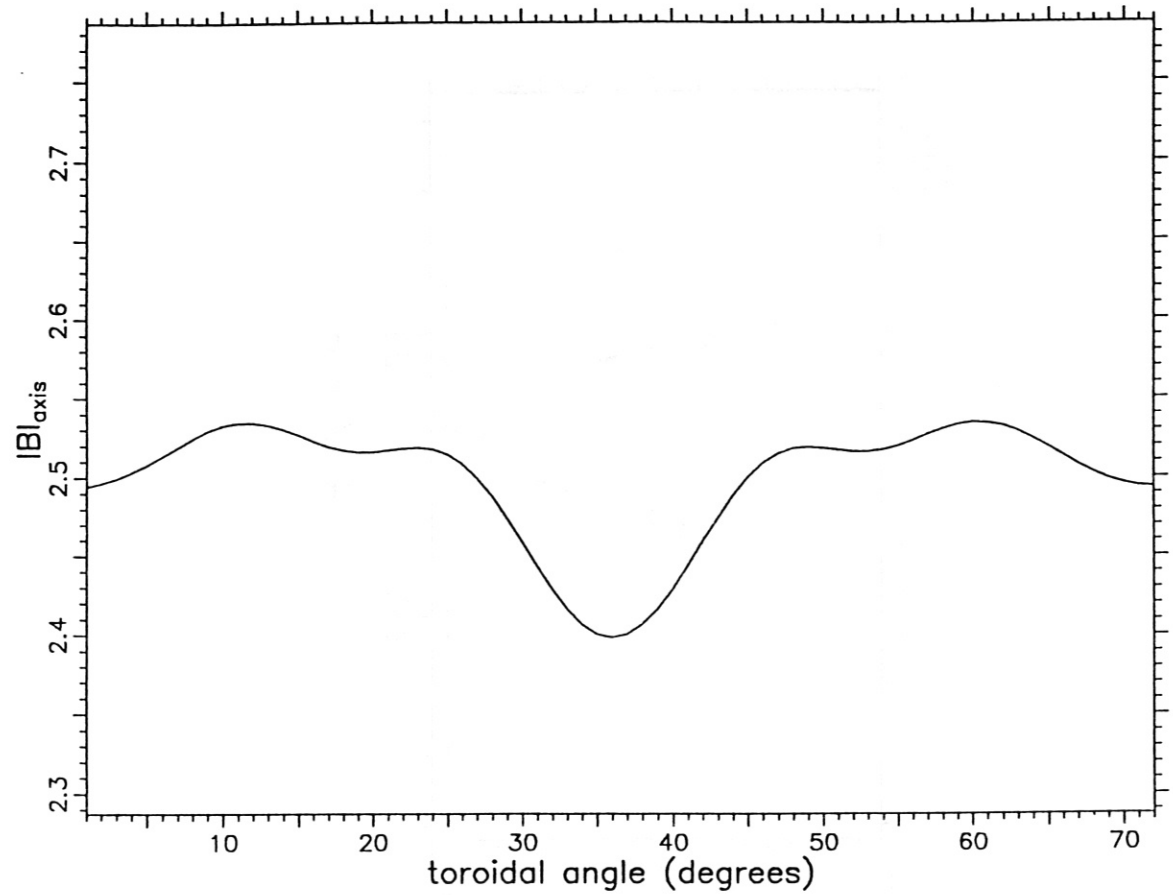
$|B|_{axis}$
2.3
2.4
2.5
2.6
2.7
10
20
30
40
50
60
70
toroidal angle (degrees)

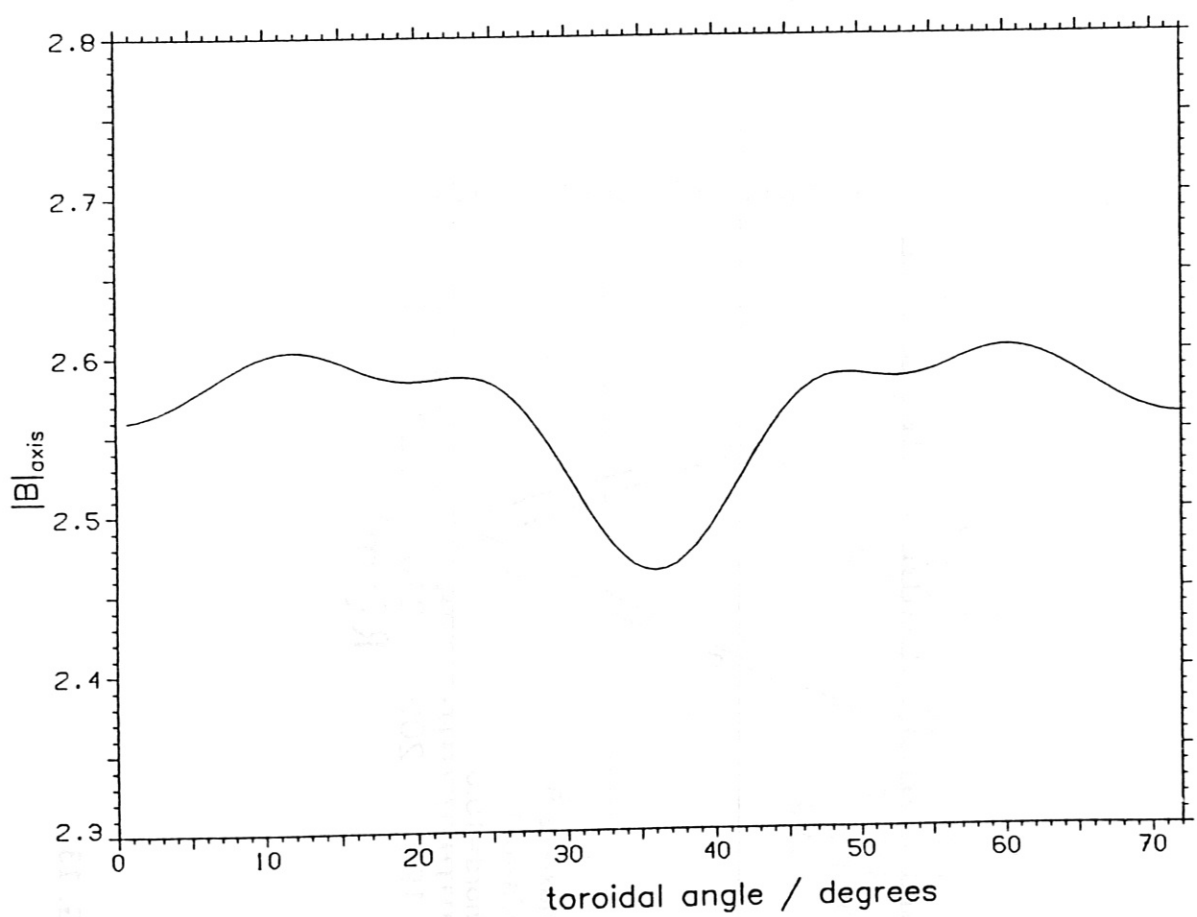
$|B|_{axis}$
2.3
2.4
2.5
2.6
2.7
2.8
0
10
20
30
40
50
60
70
toroidal angle / degrees

FIG. 14

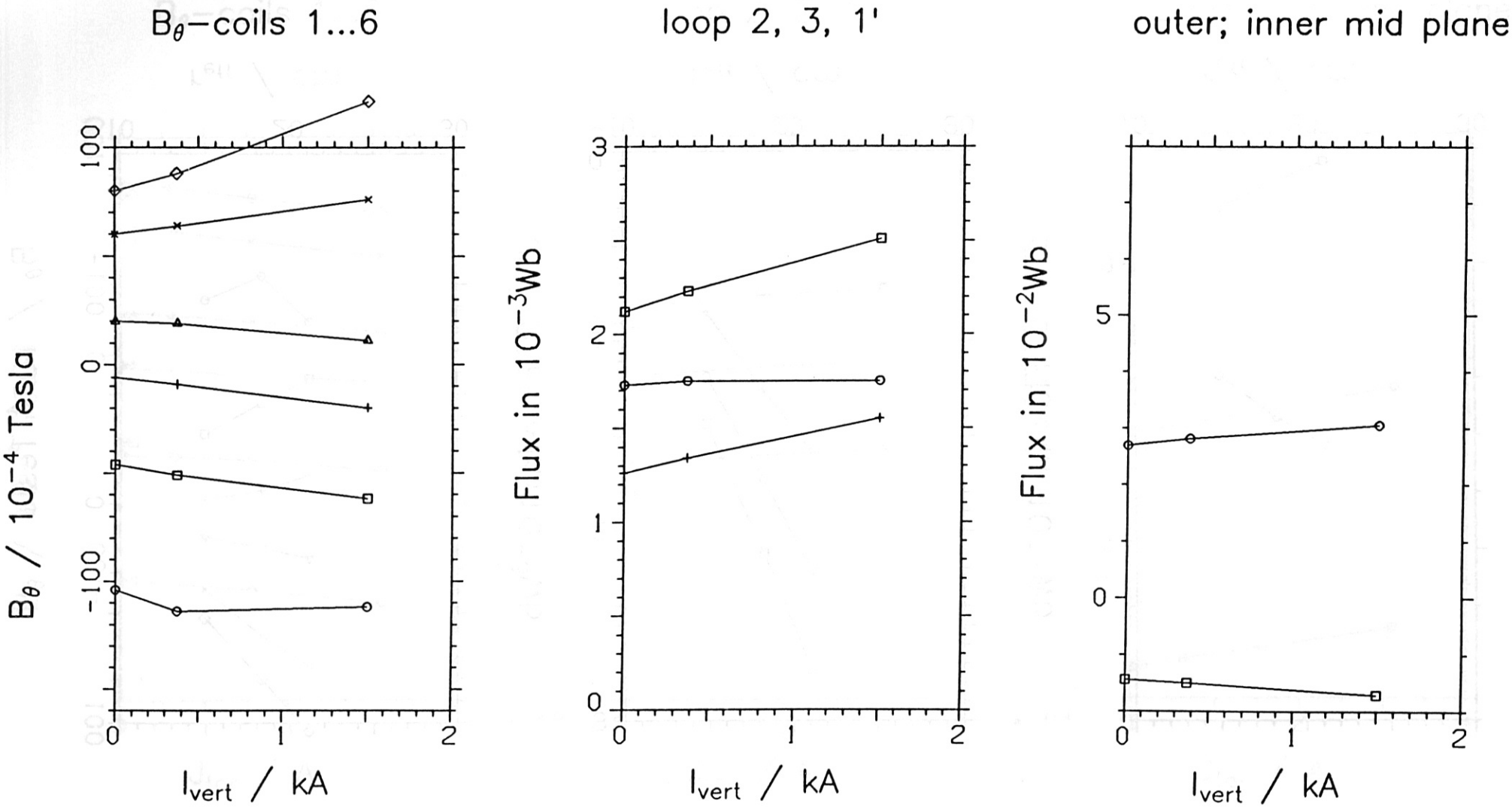
B_θ–coils 1...6
loop 2, 3, 1'
outer; inner mid plane
B_θ / 10^{-4} Tesla
100
0
-100
0
1
2
I_{vert} / kA
Flux in 10^{-3}Wb
3
2
1
0
0
1
2
I_{vert} / kA
Flux in 10^{-2}Wb
5
0
0
1
2
I_{vert} / kA

FIG. 15

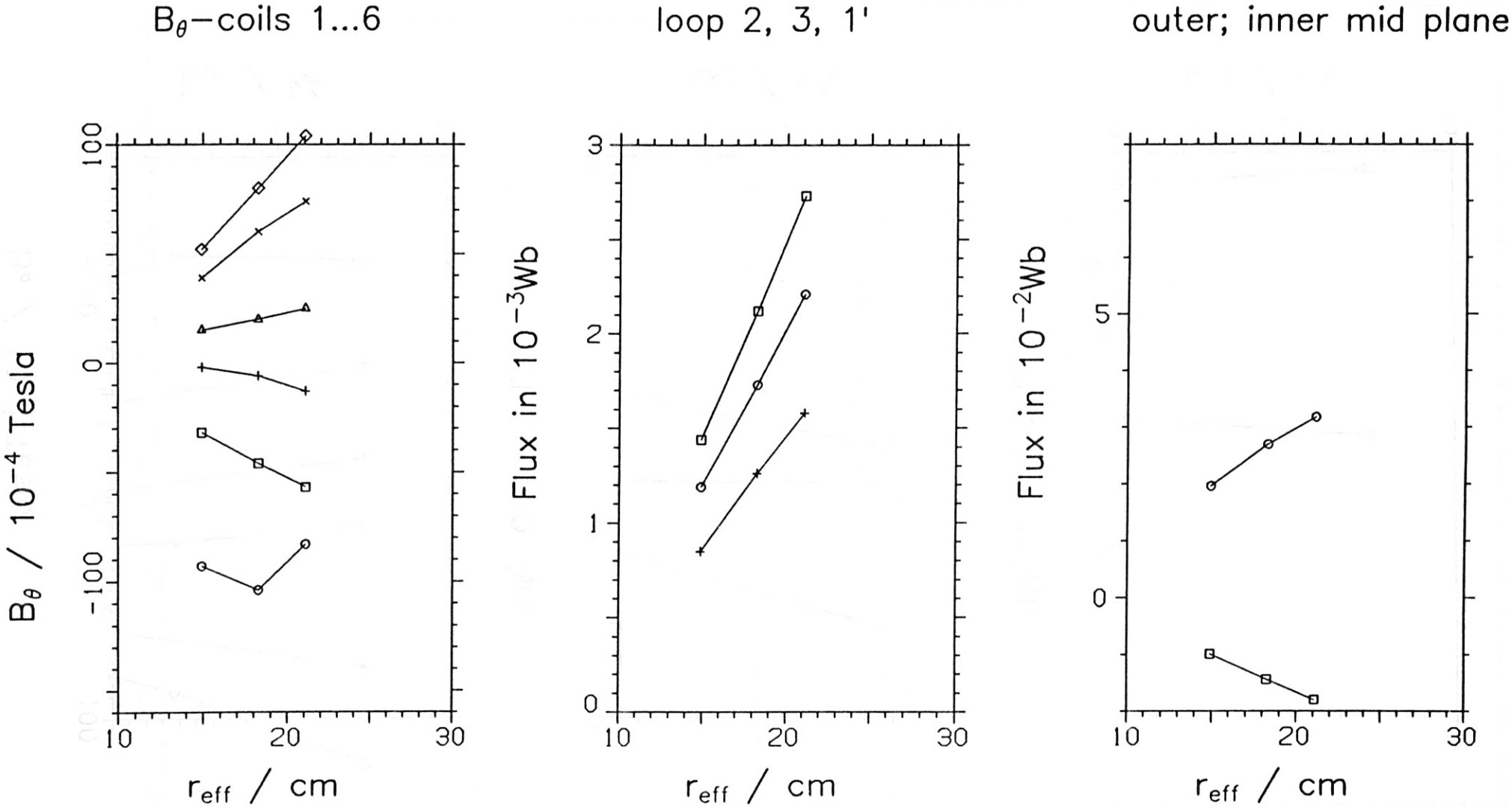
B_θ–coils 1...6
loop 2, 3, 1'
outer; inner mid plane
B_θ / 10^{-4} Tesla
100
0
-100
10
20
30
r_{eff} / cm
Flux in 10^{-3}Wb
3
2
1
0
10
20
30
r_{eff} / cm
Flux in 10^{-2}Wb
5
0
10
20
30
r_{eff} / cm

FIG. 16

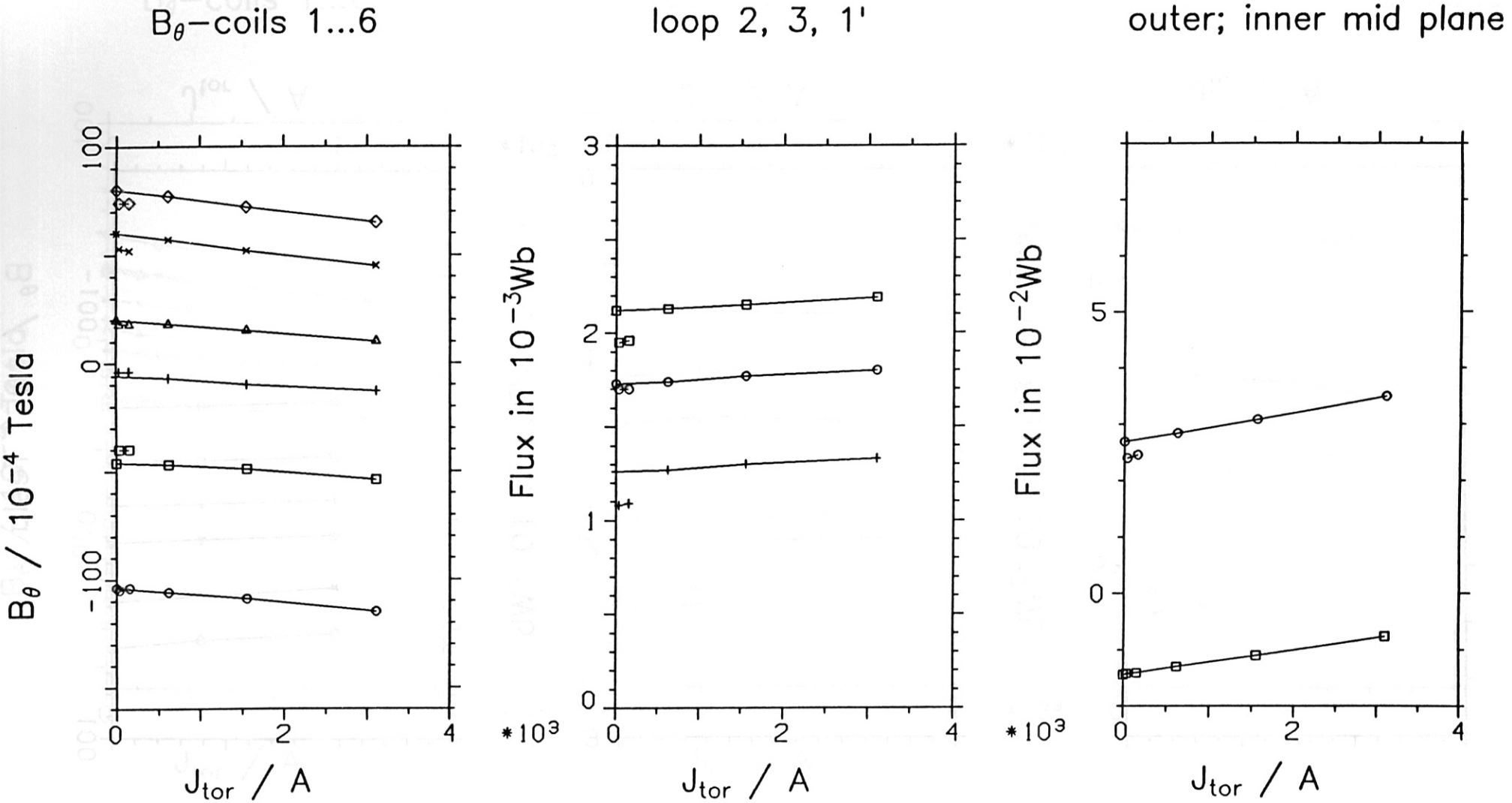
B_θ–coils 1...6
loop 2, 3, 1'
outer; inner mid plane
B_θ / 10^{-4} Tesla
100
0
-100
0
2
4
J_{tor} / A
Flux in 10^{-3}Wb
*10^3
3
2
1
0
0
2
4
J_{tor} / A
Flux in 10^{-2}Wb
*10^3
5
0
0
2
4
J_{tor} / A

FIG. 17

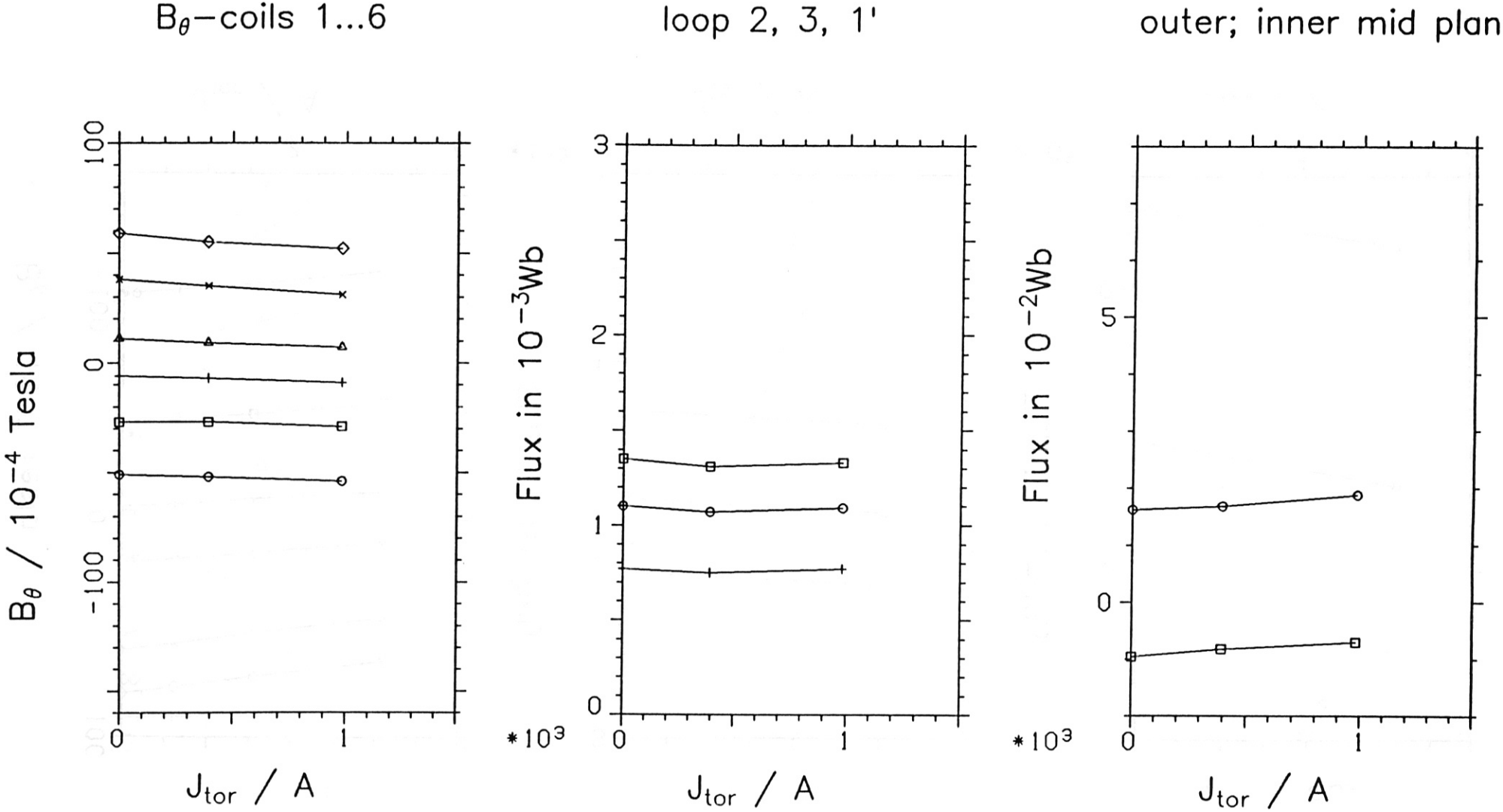
B_θ–coils 1...6
loop 2, 3, 1'
outer; inner mid plane
B_θ / 10^{-4} Tesla
100
0
-100
0
1
J_{tor} / A
Flux in 10^{-3}Wb
*10^3
3
2
1
0
0
1
J_{tor} / A
Flux in 10^{-2}Wb
*10^3
5
0
0
1
J_{tor} / A

FIG. 18

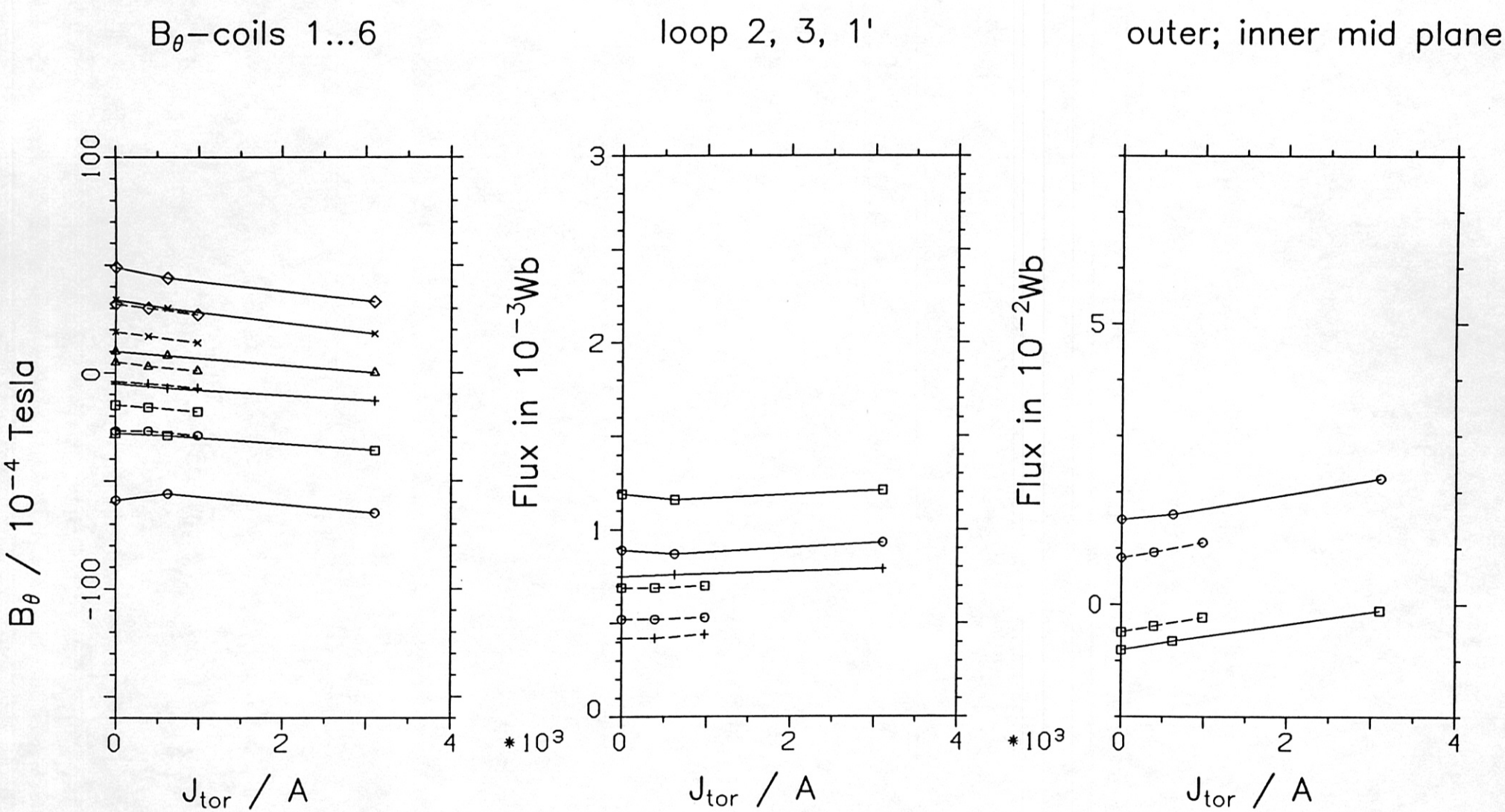
Bθ−coils 1...6
loop 2, 3, 1'
outer; inner mid plane
Bθ / 10−4 Tesla
100
0
-100
0
2
4
Jtor / A
Flux in 10−3Wb
*10³
3
2
1
0
0
2
4
Jtor / A
Flux in 10−2Wb
*10³
5
0
0
2
4
Jtor / A

FIG. 19